



POLITECNICO DI TORINO

DIMEAS – Department of Mechanical and Aerospace Engineering

College of Mechanical, Aerospace, Automotive and Production Engineering

‘Master of Science in Mechanical Engineering’

Master Degree Thesis

PRECESSIONAL SLIP AND MICRO-INCLUSION EFFECT ON FATIGUE LIFE OF BEARING ROLLING ELEMENT: AN INTEGRATED LIFE ESTIMATION MODEL THROUGH EXPERIMENTAL AND ANALYTICAL INVESTIGATION

PoliTo Supervisor : Dr. Raffaella **Sesana**

External Supervisor : Ing Irene Pessolano **Filos** (Tsubaki Nakashima Co)

Candidate : Islahuddin **Patnool**

DECEMBER 2021

Thesis submitted in Compliance with the requirements for the Master of Science Degree

I would like to dedicate this thesis to my loving parents.

For their endless love, support, and encouragement

Acknowledgment

And I sincerely express my deep sense of gratitude to my supportive and patient supervisor Prof. Raffaella Sesana for her extraordinary cooperation, invaluable guidance, and supervision. This thesis is the result of her painstaking and generous attitude.

Besides my supervisor, I genuinely acknowledge the kind assistance of my co-supervisor Ing. Irene Pessolano Filos, Industrial Ph.D. student at Tsubaki Nakashima Co., Ltd for her valuable suggestions and valuable comments throughout this research work.

I would like to express my special gratitude and thanks to the whole team from the Pineorolo plant of Tsubaki Nakashima Co., Ltd for providing all the experimental data related to my thesis work.

Abstract

In life evaluation of any mechanical component, a comprehensive numerical solver-based Life Estimation Model can replace the dependence on the expensive and often difficult to conduct experiments. Generally, these models include correction parameters to account for various operating and working conditions. Especially, in components like ball bearings, the correction factors require a complex definition. The complexity increases even more if we consider the bearing rolling element. During ball rotation, the contact point on the races remains the same but changes for the ball, mainly because of Precessional Slip and Spin motions.

The most common damage phenomenon and a serious hazard that threatens the safety of the ball bearing is Rolling Contact Fatigue (RCF). The main factor affecting sub-surface RCF is related to Non-Metallic Inclusions (NMIs), which when present near the surface of either contacting bodies in rotation lead to failure. These NMIs usually get stressed whenever they pass through the ball-race contact region. This inclusion loading frequency is largely influenced by the slip and precession motion of the ball. An Integrated Numerical-based Life Estimation Model for Bearing rolling element under the influence of Precessional Slip and Micro-Inclusion effects is proposed.

Contents

1. Introduction	1
2. Literature Review.....	8
2.1 Rolling Contact Fatigue.....	8
2.1.1 Factors that influence RCF Life.....	9
2.2 Bearing Life Theory	11
2.2.1 Hertz Contact Stress Theory	11
2.2.2 Equivalent Load	12
2.2.3 Fatigue Limit.....	13
2.2.4 L10 Life.....	14
Bearing Life Models.....	16
2.3.1 Lundberg-Palmgren Model	17
2.3.2 Ioannides-Harris Model	17
2.3.3 Zaretsky Model.....	19
3. Ball Motions and Precessional Slip Model	26
3.1 Precessional Slip	28
3.2 Ball Local Reference Frame.....	30
3.3 Ball Angular Velocity with Precession.....	31
3.4 Ball-race contact velocity	36
3.5 Ball-Race Slips.....	37
3.6 Basic Speed Ratio with Precession.....	37
3.7 Spin-Precession Ratio.....	38

3.8 Transverse Precessional Slip.....	39
3.9 Ball Spin Frequency	39
3.10 Transverse Slip Ratio	41
3.11 Inclusion Loading Frequency.....	42
4. Non-Metallic Inclusions	44
4.1 Types of Inclusions	46
4.2 Factors influencing stress peak.....	48
4.2.1 Dimension.....	48
4.2.2 Depth	51
4.2.3 Shape.....	52
4.2.4 Chemical composition	56
4.2.5 Configuration	57
5. Experimental Tests	59
5.1 Rotating Bending Fatigue Test.....	61
5.2 Test rig for fatigue testing of balls.....	65
5.4 Fracture Analysis	73
5.4.1 Failed ball - Test Rig.....	73
Failed Specimen - Rotating bending test.....	76
6. Micro-Inclusion Model.....	77
6.1 Eshelby-Mura Model	78
6.1.1 Equivalent Inclusion Method	79
6.2 Matlab Solver	81
6.3 Statistics of Extreme Values Method.....	83
6.3.1 Cleanliness Analysis	85

6.3.2	Experimental data.....	86
7.	Integrated Life Model.....	90
7.1	Integrated Life Model-Relating Life with Precessional slip and Inclusion effect.....	91
7.2	Integrated Numerical Solver.....	93
8.	Results and Discussions.....	94
8.1	Experimental Results.	94
8.1.1	Statistics of Extreme Values Method.....	94
8.1.2	Four-Point Rotating Bending Test on Specimen.....	96
8.1.3	Fatigue Tests on Bearing Balls.....	98
8.2	Integrated Numerical Solver.....	101
8.2.1	Ball Local Reference Frame	101
8.2.2	Ball Angular Velocity with Precession.....	102
8.2.3	Surface Velocities at Ball-Race contact	103
8.2.4	Precessional Slip and Pure Spin at Ball-Race Contact.....	104
8.2.5	Basic Speed Ratio with Precession.....	104
8.2.6	Spin-Precession Ratio.....	105
8.2.7	Transverse Precessional Slip	106
8.2.8	Ball Spin Frequency	107
8.2.9	Transverse Slip Ratio.....	108
8.2.10	Inclusion Loading Frequency.....	110
8.2.11	Dynamic load capacity&Ball-Race Conformity effects	110
8.2.12	Equivalent Tresca stresses - failed specimens	112
8.2.13	Equivalent Tresca stresses - Failed balls.....	113

8.2.14 Calculated Equivalent Loads.....	114
8.2.15 Predictions vs Actual Ball Life.....	116
9. Conclusions.....	118
10. Future Works.....	120
11. Bibliography.....	122

List of Figures

Fig 1 Ball-race model for point contact.....	16
Fig 2 Ball-race conformity in Angular-contact ball bearing.....	22
Fig 3 Ball Precession:	29
Fig 4 Contact Geometry.....	30
Fig 5 Precession Geometry	32
Fig 6 Bearing not running	33
Fig 7 Bearing counter-rotating with ball precession, illuminated at δ •	33
Fig 8 Bearing counter-rotating with ball precession, illuminated at p ...	34
Fig 9 Alluminates type	48
Fig 10 Oxides type.....	48
Fig 11 Stress Threshold for inclusion size of 0.5 μm radius	50
Fig 12 Stress Threshold for inclusion size of 50 μm radius	50
Fig 13 Effect of depth (contact half-width) on Tresca Stress	52
Fig 14 Influence of Aspect ratio (y/x) on stress peak	53
Fig 15 % Stress increment for ratio $y/x = 1$	54
Fig 16 % Stress increment for ratio $y/x = 2$	55
Fig 17 % Stress increment for ratio $y/x = 10$	55
Fig 18 Depth Threshold.....	58

Fig 19 Rotating bending machine.....	61
Fig 20 Raw material and final standard specimen	62
Fig 21 Standard specimen geometry.....	63
Fig 22 Four-Point Rotating Bending Test: Loading Condition	64
Fig 23 Test rig benches for ball bearing test.....	66
Fig 24 Test Rig close-up.....	67
Fig 25 Test rig bench with every component labeled.....	68
Fig 26 Test rig control computer.....	69
Fig 27 Test Bearing modification	70
Fig 28 Stereomicroscope	73
Fig 29 Gauge Meter.....	74
Fig 30 Scanning Electron Microscope (SEM)	75
Fig 31 Standard inspection area 0.5 mm ²	87
Fig 32 Examples of Inclusions found	87
Fig 33 Estimation of the maximum inclusion size in a volume of 100Cr6 steel by the SEV method.....	95
Fig 34 Case 3: Micro-inclusion crater in the specimen (63 <i>x</i> , 200 <i>x</i> , 800 <i>x</i>)	98

List of Tables

Table 1 Values of coefficients of thermal expansion α , Young's modulus E, and Poisson's ratio ν	47
Table 2 Effect of Inclusion dimension	49
Table 3 Effect of inclusion depth on stress increment.....	51
Table 4 Effect of Shape on the stress increment	54
Table 5 Effect of chemical composition on stress peaks.....	57
Table 6 Data collected after Inspection.....	88
Table 7 Parameters used in SEV method	94
Table 8 Probability that the largest inclusion is no larger than a fixed <i>Areamax</i>	96
Table 9 Results of fatigue testing on specimens.....	97
Table 10 Test rig - Ball fatigue and failure inspection results	99
Table 11 Ball Reference System	101
Table 12 Ball Precessional Velocity.....	102
Table 13 Ball and Races surface velocities	103
Table 14 Slip and Spin velocities at Ball-Race contact.....	104
Table 15 Bearing speed and speed ratio.....	105
Table 16 Influence of spin and precession on ball velocity.....	105

Table 17 Transverse Precessional Slip Fields at Ball-Race contacts....	106
Table 18 All the fundamental defect frequencies.....	107
Table 19 Transverse slip amplitude to ball's surface velocity	108
Table 20 Inclusion Loading Frequency (I_L)	110
Table 21 Dynamic load capacity and Bearing life factor	111
Table 22 Equivalent Tresca Stresses	112
Table 23 Corrected Equivalent Tresca stresses - Failed balls	113
Table 24 Calculated Equivalent Loads.....	114
Table 25 Bearing ball life Comparisons.....	116

Chapter 1

Introduction

Predictions operating Life of angular contact ball bearings are currently based on largely unconfirmed theory. Life evaluation by rig testing a large number of nominally identical bearings to failure under simulated operating conditions is a sure but expensive method. For design purposes, therefore, a requirement exists for a comprehensive and substantiated method of life prediction. A numerical-based model can serve as a tool that replaces the dependence on expensive and often difficult to conduct experiments. However, the model must be accurate enough to substitute the experiments. This Thesis concerns development of such an Integrated Life Estimation Model for ball bearing.

Generally, these life models developed to estimate the life of any component are validated by comparing fatigue tests under different loading conditions. Often, introducing correction parameters becomes a necessity to account for various working conditions. Especially in components like bearings, the correction factors require a complex definition to account for all possible effects of working conditions such as temperature, rotational speed, and lubrication, to name a few. It becomes even more complex, in the

case of the bearing rolling element. Case in point, during rotation of the bearing rolling element, the contact point on the races remains the same but changes for the ball, mainly because of Precession and Spin motions. It is noteworthy that most of the research investigating the fatigue life of bearing balls conducts tests on specimens like plates and rods (1) (2).

In optimal working conditions, the most common damage phenomenon and a serious hazard that threatens the safety of ball bearings is Rolling Contact Fatigue (RCF). RCF involves surface pitting and subsurface spalling. The main factor affecting sub-surface RCF is related to Non-Metallic Inclusions (NMIs), where Hertz contact shear stress is maximum (3). I.e., For two bodies in contact (in our case: bearing ball and raceway), the superficial and sub-superficial stress distribution is estimated by Hertz's theory. If NMIs are present in any of these contacting bodies, specifically near the surface of either contacting body, they lead to Rolling Contact Fatigue. These inclusions act as stress risers promoting crack initiation, propagation, and eventually failure.

. To consider the effect of Non-Metallic Inclusions on the bearing life, it is important to determine how often the micro-inclusion is stressed. The sub-surface micro-inclusion is usually stressed whenever it passes through the contact region i.e whenever it is positioned below the contacting surface of either bodies at the ball-race contact. In the case of bearing rolling elements, the sub-surface micro-inclusion does not always pass through the contact region due to Slip and Precession motions. Hence, to estimate the actual contacts occurring between the race and the point of the ball surface below which the microinclusion is present becomes complicated.

The Precessional motion of the ball is defined as the change in the orientation of the rotational axis of the ball. In an appropriate reference frame, it can be defined as a change in the first Euler angle, whereas the third Euler angle defines the rotation itself. The nature of the frictional

forces and moments applied to an angular contact bearing's rolling element (ball) should be examined in terms of slip, spin, and precession. The spin motion is vital in the discussion of the ball's precessional motion.

Several mathematical models have been proposed over the years to estimate the life of bearing components under RCF. These models can be classified into probabilistic engineering models and deterministic research models. The engineering models are largely empirical and include variables that are obtained from extensive experimental testing. They neither consider the details of the constitutive behavior of materials under contact loading, nor the residual stress and strain computations in the contact areas.

On contrary, the research models are purely theoretical and certainly require complete stress-strain behavior information about the materials in contacts. They are used in conjunction with a material failure model. However, these models are usually confined to a specific aspect of the failure process, e.g., either only the crack initiation part or only the crack propagation part. Most of the previous work concerning estimation of life of the rolling bearing is confined to Empirical results due to the special nature of Rolling Contact Fatigue. It's inability to relate to classical Fatigue.

In the current Thesis, A review is presented outlining the theory and application of rolling-element bearing life prediction from that of A. Palmgren, 1924, W. Weibull, 1939, G. Lundberg and A. Palmgren, 1947 and 1952, E. Ioannides and T. Harris, 1985, and E. Zaretsky, 1987. Their respective Bearing Life Models are discussed in detail. Zaretsky Model was considered for bearing life estimation. The life formulation from the model is modified to include the correction to account for ball-race conformity. The Zaretsky life model is further modified, to consider the spin and precession motion done by the ball during the shaft rotation to estimate the actual contact occurring between the race and the point on the ball surface below which the micro-inclusion is present.

All the parameters concerning bearing rolling elements slip, spin, and precession are examined in detail. A reference system modeling the ball local reference frame is presented. For the ball precessing in counter-rotation, its angular velocity vector is made of two oblique components, spin along the hole axis and precession of the hole axis. These include the precession angle. The Ball angular velocity with precession motion specified for the fixed reference frame is formulated as a function of time. The surface velocities at ball-race contact (both outer and inner) are determined along with respective radius vectors.

The slip velocities at ball-race contact in the presence of precession and spin velocities in ordinary conditions (pure spin) are estimated. The ball-race slips are defined as race minus ball surface velocity. The differences between Slip Velocities with and without Precession (pure spin) at Ball-Race contact are compared. The basic speed ratio with precession was generalized using the First-order bearing theory. The total bearing speed was estimated. To analyze the influence of the oblique components: spin and precession on the ball angular velocity, the spin-precession ratio was determined.

For the precessional motion to occur, ball precession requires a time-varying transverse precessional slip field at outer and inner ball-race contact. In other words, Transverse Precessional Slips must form at both inner and outer ball-race contact across the rolling direction for the precessional motion to occur. The formulation for estimating the transverse precessional slip along the rolling direction is specified. The concept of Ball Spin Frequency was employed to statistically determine how often the inclusion is loaded i.e the frequency with which the surface point near the inclusion contacts the outer and inner race.

The amount of slip a ball undergoes and how it is linked to the complete revolution of the ball in one shaft cycle is given by the ratio of transverse

slip amplitude to ball surface velocity in the motion. This ratio of transverse slip done by the ball while doing a complete rotation around the principal axis is modeled for ball-race contact, in presence of retainers as per our experimental condition. Assuming that the transverse slip is not random, but always in the same direction of rotation, the micro-inclusion loading frequency. i.e., how frequently the inclusion in the ball contacts the raceways is determined using Inclusion loading frequency.

To account for the Non-Metallic Inclusions effect on the bearing life, a review on types of inclusions and the factors influencing the stress peaks such as inclusion dimensions, depth, shape, chemical composition, and configuration is presented. Given the location, dimension, aspect ratio, and composition of the micro-inclusion, the stress field surrounding the micro-inclusion are computed using Eshelby-Mura Model. The inhomogeneity problem and inclusion problem were co-related using the Equivalent Inclusion Method. The distribution of the non-metallic inclusion in the material matrix was identified using the Statistics of Extreme Values Method.

Experimental investigations were carried out to detect the micro-inclusion and characterize them based on the factors influencing their stress peaks. RCF test campaigns using a dedicated test rig were conducted to evaluate the fatigue life of the bearing rolling element. A rotating bending fatigue test was performed on a standard specimen to detect the micro-inclusion from which the fracture initiates. On the failed specimens and the failed balls coming from bending test and test rigs respectively, the Fracture Analysis was conducted. The Stereo-microscope inspection, measurements from the Gauge meter, and the Scanning Electron Microscope Analysis investigate the origin of the fracture along with the estimation of the dimensions, shape, chemical composition, and depth of the inclusion.

All the experimental activities were carried out at Tsubaki Nakashima Co., Ltd. Tsubaki Nakashima Company manufactures and sells steel balls and precision products worldwide. Especially the group is a global leader in the manufacturing and production of Rolling contact elements such as premium quality precision balls and rollers, cages, and sheet metal parts. Pinerolo plant, where experiments were conducted, is specialized in the manufacturing and production of the bearings balls.

An Integrated Life Estimation Model with a dedicated Numerical Solver is developed to investigate the relationship between the Precessional Slip and the Bearing life in the presence of the Micro-inclusion. The Zaretsky's bearing life formulated was modified to include the influence of precessional slip and micro-inclusion effect. All the conditions leading to precessional slip such as transverse slip, ball spin frequency, and inclusion loading frequency were calculated using the solver based on the experimental data with bearing geometrical parameters. From the fracture analysis data regarding the inclusion's composition, dimensions, depth, and aspect ratio, the corresponding corrected equivalent Tresca stresses were calculated using Eshelby's code.

The parameter crucial in relating the precessional slip and micro-inclusion effect with the bearing rolling-element life is the "Equivalent dynamic Load" present in the bearing life formulation of the Zaretsky Model. In contrast to the nominal equivalent dynamic load, a new equivalent load including the average normal force acting on the ball in the presence of micro-inclusion while undergoing transverse precessional slip was introduced. The ball-race conformity effects were also taken into account.

Finally, the bearing life predictions are calculated. Nominal bearing life assuming the absence of the precessional slip and the micro-inclusion effect corresponding to nominal dynamic load is calculated. Likewise, bearing life is estimated in the presence of micro-inclusion under the influence of the

precessional slip, corresponding to dynamic load including average normal force. These predicted ball lives by the solver are compared with the experimental cycles of failure coming from ball fatigue tests to validate our Integrated Model. The thesis ends with concluding remarks. All the reference sources are cited and listed in the Bibliography section.

Thesis Statement: To develop an Integrated Numerical-based Life Estimation Model for the Bearing rolling element under the influence of Precessional Slip and Micro-Inclusion effects.

Chapter 2

Literature Review

2.1 Rolling Contact Fatigue

Rolling Contact Fatigue (RCF) is the most common damage phenomenon and a serious hazard that threatens the safety of mechanical components such as ball bearings involving rolling or sliding contact. Systems undergoing RCF are subjected to material failure due to the application of repeated stresses in a small volume (typical bearing contact widths are in the order of 200-1000 μm) (4). RCF generates a multiaxial state of stress which makes estimation of component's life complex.

RCF predominantly involves Surface Pitting and Sub-Surface Spalling. Surface-induced RCF failures (Pitting) occur due to surface distresses such as dents, fretting scars, etc on the surface of contacting bodies. Surface-originated Pitting can be mitigated with proper lubricant and Elastohydrodynamic Lubrication. Sub-Surface Spalling is principal if the contacting surfaces are relatively smooth. It typically appears near an Inclusion or material inhomogeneity within the material domain (5). The main factor affecting sub-surface RCF is related to Non-Metallic Inclusions,

where Hertz contact shear stress is maximum (3). These inclusions act as stress risers promoting crack initiation and propagation. Improved steel cleanliness can control Inclusions and Oxides to an extent. However, inclusions cannot be completely removed.

2.1.1 Factors that influence RCF Life

RCF life depends on many factors such as

- Contact Pressure
- Material properties
- Lubricant properties
- Surface roughness
- Relative slip during the rotation between the elements
- Microstructure
- Cleanliness Condition
- Residual stresses

Cleanliness would be of more importance since we are analyzing the effect of micro inclusions on the bearing fatigue life. Several Parameters such as Dimensions, Shape, Depth, Chemical Composition, and Configuration characterize the micro-inclusions.

Inclusion size affects stress distribution around inhomogeneity. i.e., stress volume increases as the inclusion size increases. Although, maximum values of stress (like max von mises stress) does not strongly depend on inclusion size as confirmed by the Eshelby model (6). Depending on the chemical composition, inclusions have different shapes. Typically, Al_2O_3 inclusions have a spheroidal or ellipsoidal shape while Nitrides and Carbides are sharper. The effect of the ellipsoidal-shaped inclusions is explained in later chapters. Within the component, volume inclusion appear at random depths. If the inclusion is positioned too far from the surface, its stress

concentration effect can be neglected. However, if the inclusion is located at a critical depth (depends on the geometrical parameters at the contact), it is detrimental for the fatigue life (6).

The chemical composition (oxides, nitrides, carbides, silicates, etc.) of the inclusion are influenced by the Young Modulus and Poisson Ratio. Most non-metallic inclusions have an elastic modulus higher than the matrix one. i.e. the maximum von Mises stress or Tresca stress will increase as the difference between two moduli increases. This is similar in the case of Poisson's ratio as well. Inclusion Configuration (pairs, clusters, and stringers) largely affects the endurance limit of the bearing material. The approximation of the uniform applied stresses becomes invalid when two or more inclusions are next to each other within a certain distance limit. As a result, the Eshelby model should be revised (7). This Eshelby model revision can be seen in the later chapters.

2.2 Bearing Life Theory

Foundation for bearing life prediction.

2.2.1 Hertz Contact Stress Theory

In 1924, Arvid Palmgren published a paper (8) that laid the foundation for Lundberg-Palmgren's theory (9). The paper was missing certain key aspects which did not allow for a comprehensive Rolling-element Bearing Life Theory. The first was the ability to calculate the subsurface principal stresses and the shear stresses below the Hertzian contact of a ball on a nonconforming race. The second was a comprehensive life theory that would fit the observations of Palmgren. Palmgren discounted Hertz's contact stress theory (10) and depended on the load-life relation for the ball and roller bearings, based on tests carried out at SKF Sweden that began in 1910 (11). Zaretsky discusses the 1924 Palmgren work in (12).

Palmgren had no confidence in the ability of the Hertzian equations to accurately predict rolling bearing stresses. Palmgren later recanted his doubts about the validity of Hertz's theory and incorporated the Hertz contact stress equation in his 1945 book (8). In their 1947 paper (9), Lundberg and Palmgren state that Hertz's theory is valid under the assumptions that the contact area is small compared to the dimensions of the bodies, and the frictional forces in the contact areas are neglected. For ball bearings (our case), with close conformity between rolling elements and raceways, these conditions are only approximately true.

Lundberg and Palmgren exhibited a great deal of insight as to what other variables modify the resultant shear stresses calculated from Hertz's theory. They state (9), *“No one yet knows much about how the material reacts to the complicated and varying succession of (shear) stresses which then occur, nor is much known concerning the effect of residual hardening*

stresses or how the lubricant affects the stress distribution within the pressure area. Hertz's theory also does not treat the influence of those static stresses which are set up by the expansion or compression of the rings when they are mounted with tight fits”.

These effects are now understood, and life factors are currently introduced to account for them to more accurately predict bearing life and reliability (13).

2.2.2 Equivalent Load

Palmgren (8) recognized that it was necessary to account for combined and variable loading around the circumference of a ball bearing. He proposed a procedure to establish functions for the service life of bearings under purely radial load and to establish rules for the conversion of axial and simultaneous effective axial and radial loads into purely radial loads. Palmgren used Stribeck’s equation (14) to calculate stress on the maximum radially loaded ball-race contact in a ball bearing. The equation attributed to Stribeck by Palmgren is as follows:

$$k = \frac{5 Q}{Z d^2} \quad (2.1)$$

where Q is the total radial load on the bearing, Z is the number of balls in the bearing, d is the ball diameter, and k is Stribeck’s constant.

Palmgren modified Stribeck’s equation to include the effects of speed and load as well while modifying the ball diameter relation. Palmgren (8) states, *“It is probably impossible to find an accurate and, at the same time, simple expression for the ball pressure as a function of radial and axial pressure...”* According to Palmgren, *“Adequately precise results can be obtained by using the following equation:*

$$Q = R + y A \quad (2.2)$$

where Q is the imagined, purely radial load that will yield the same service life as the simultaneously acting radial and axial forces, R is the actual radial load, and A is the actual axial load". For ball bearings, Palmgren presented values of y as a function of Stribeck's constant k . Palmgren stated that these values of y were confirmed by test results (8).

By 1945, Palmgren (15) modified Eq. 2.2 is as follows:

$$Q = P_{eq} = X F_r + Y F_a \quad (2.3)$$

where P_{eq} is the equivalent load, F_r is the radial component of the actual load, F_a is the axial component of the actual load, X is the rotation factor, Y is the thrust factor of the bearing.

The rotation factor X is an expression for the effect on the bearing capacity of the conditions of rotation. The thrust factor Y is a conversion value for thrust loads (15).

2.2.3 Fatigue Limit

Palmgren (8) states that bearing "*limited-service life is primarily a fatigue phenomenon. However, under exceptional high loads, there will be additional factors such as permanent deformations, direct fractures, and the like....*". Starting with the assumption that the material has a certain fatigue limit, meaning that it can withstand an unlimited number of cyclic loads on or below a certain, low level of load, the service life curve will be asymptotic. Since, moreover, the material has an elastic limit and/or fracture limit, the curve must yield a finite load even when there is only a single load value, meaning that the number of cycles equals zero.

If we further assume that the curve has a profile of an exponential function, the general equation for the relationship existing between load and number of load cycles before fatigue would read:

$$k = C (a n + e)^{-x} + u \quad (2.4)$$

where k is the specific load or Stribeck's constant, C is the material constant, a is the number of load cycles during one revolution at the point with the maximum load exposure, n is the number of revolutions in millions, e is the material constant that is dependent on the value of the elasticity or fracture limit, u is the fatigue limit, and x is an exponent.

2.2.4 L_{10} Life

According to Palmgren in equation 1, “*This exponent x is always located close to $1/3$ or 0.3. Its value will approach $1/3$ when the fatigue limit is so high that it cannot be disregarded, and 0.3 when it is very low.*” Palmgren reported test results that support a value of $x = 1/3$. Hence, Eq. (0.4) can be written as

$$L \text{ (millions of stress cycles)} = \left(\frac{C}{k - u} \right)^3 - e \quad (2.5)$$

The value e suggests a finite time below which no failure would be expected to occur. By letting $e = 0$ and eliminating the concept of a fatigue limit for bearing steels, Eq. (0.5) can be rewritten as

$$L \text{ (millions of race revolutions)} = \left(\frac{C Z d^2 / 5}{Q} \right)^3 \quad (2.6)$$

In Eq. (0.6), by letting $f_c = C/5$ and $Peq = Q$, the 1924 version of the dynamic load capacity C_D for a radial ball bearing would be

$$C_D = f_c Z d^2 \quad (2.7)$$

For ball bearings, Palmgren empirically modified the dynamic load capacity C_D

$$C_D = f_c \frac{i d Z^{2/3} \cos \beta}{1 + 0.02 d} \quad (2.8)$$

f_c is a material-geometry coefficient, i number of rows of rolling elements (balls or rollers), d ball or roller diameter, Z number of rolling elements (balls or rollers) in row i , β bearing contact angle.

and Eq. (0.6) becomes

$$L_{10} = \left(\frac{C_D}{P_{eq}} \right)^3 \quad (2.9)$$

where L_{10} is the life in millions of inner-race revolutions, at which 10 percent of a bearing population will have failed and 90 percent will have survived. This is also referred to as 10-percent life or L_{10} life.

The L_{10} life, or the time that 90 percent of a group of bearings will exceed without failing by rolling-element fatigue, is the basis for calculating bearing life and reliability today.

In their 1952 paper (16) Lundberg and Palmgren modified the value of the exponent .i.e load-life exponent p for roller bearings to 10/3 from 4, while it remained the same 3 for ball bearing.

2.3 Bearing Life Models

The life of the bearings is governed by Rolling Contact Fatigue since fatigue is the most predominant mode of failure in bearing rolling elements. Several mathematical models have been proposed over the years to estimate the life of bearing components under RCF. These models can be classified into probabilistic engineering models and deterministic research models. The engineering models are largely empirical and include variables that are obtained from extensive experimental testing. They neither consider the details of the constitutive behavior of materials under contact loading, nor the residual stress and strain computations in the contact areas.

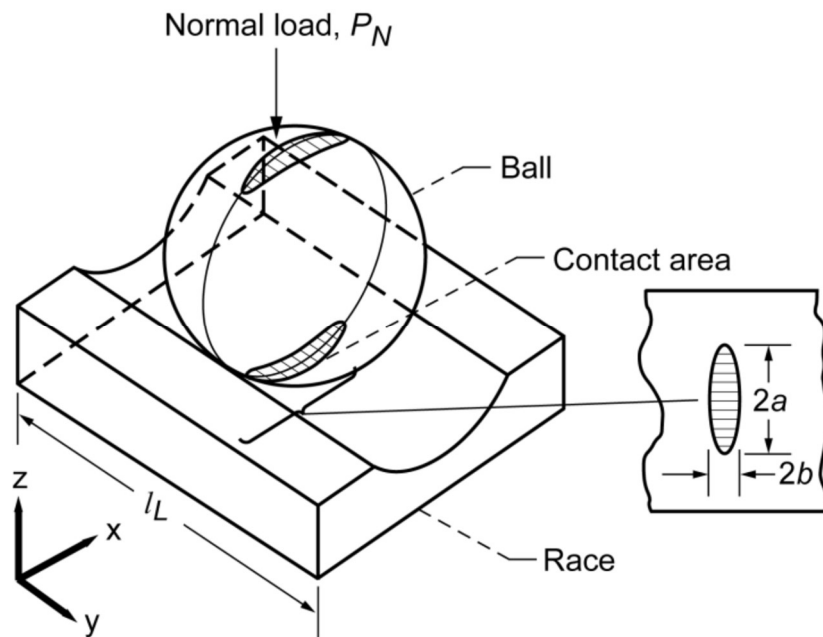


Fig 1 Ball-race model for point contact

On contrary, the research models are purely theoretical and certainly require complete stress-strain behavior information about the materials in contacts. They are used in conjunction with a material failure model. However, these models are usually confined to a specific aspect of the failure process, e.g., either only the crack initiation part or only the crack

propagation part. Most of the previous work concerning estimation of life of the rolling bearing is confined to Empirical results due to the special nature of Rolling Contact Fatigue. It's inability to relate to classical Fatigue.

2.3.1 Lundberg-Palmgren Model

As we have already discussed, Lundberg and Palmgren (9) provided the first theoretical formulation of the bearing life model to predict rolling-element bearing fatigue life by applying the Weibull statistical strength analysis. They assumed that the crack initiates at the subsurface to a particular depth as a result of maximum orthogonal shear stress and a weak point in the material. Such weak points were statistically distributed in the material. The Weibull statistical strength theory was applied to the stressed volume in a pure Hertzian contact to obtain the probability of survival of the volume from subsurface-initiated fatigue.

They formulated the relationship between individual component life and system life. Bearing being a system of multiple components, each with a different life, the life of the bearing is different from the life of the individual bearing elements. The L_{10} bearing system life, where 90 percent of the population survives, can be expressed from equation 2.9 :

$$L_{10} = \left(\frac{C_D}{P_{eq}} \right)^p \quad (2.10)$$

where p is the load-life exponent (3 for ball bearings and $\frac{10}{3}$ for roller bearing), C_D is the dynamic load capacity for a rolling element, P_{eq} is the equivalent load.

2.3.2 Ioannides-Harris Model

Ioannides and Harris (17) introduced Fatigue limiting shear stress τ_u in the Lundberg and Palmgren's bearing life model which applied the Weibull

analysis to the prediction of rolling-element bearing fatigue life. They modified the Lundgren-Palmgren equation to include the “fatigue-limiting” load P_u which is a function of τ_u i.e, $P_u = f(\tau_u)$. For critical shearing stress, Ioannides and Harris chose the von Mises stress.

From the above, Eq. (2.10) can be rewritten as

$$L_{10} = \left(\frac{C_D}{P_{eq} - P_u} \right)^p \quad (2.11)$$

When $P_{eq} < P_u$, bearing life is infinite and no failure would be expected. But when $P_u = 0$, life is the same as that for Lundberg and Palmgren.

The concept of a fatigue limit for rolling-element bearings was first proposed in 1924 by Palmgren (Eq. (2.11)) (8). It was later abandoned by him first in 1945 (15) and then again with Lundberg in 1947 (16). In 1985, Ioannides and Harris (18) applied Palmgren’s concept of a fatigue limit to the Lundberg-Palmgren equations. The ostensible reason why Ioannides and Harris used the fatigue limit, was to replace the material and processing life factors that are used as life modifiers in conjunction with the bearing lives calculated from the Lundberg-Palmgren equations.

There are several issues associated with the use of a fatigue limit for rolling element bearing. For one, a fatigue limit does not exist for bearing steels. This was later reported in a paper by Tosha et al. (19) where results of rotating bending fatigue experiments for through-hardened AISI 52100 steel at very low-stress levels showed conclusively that a fatigue limit does not exist for this bearing steel.

Later publications by the ASME (20) and the ISO (21) (22) include fatigue limit along with the effects of ball-race conformity on bearing life for calculating the life of rolling-element bearings. These methods do not, however, include the effect of ball failure on bearing life.

The concept of a fatigue limit load (*bearing load under which the fatigue stress limit is just reached in the most heavily loaded raceway contact*) is introduced in the new ISO rating methods (22). This fatigue load limit is proportional to the fatigue limit load raised to the 3rd power for ball bearings (point contact). These differing values of load would result in a 128-percent higher load below which no fatigue failure would be expected to occur (23) using ISO 281:2007 (21) than ASMELIFE (20).

The effects of using different values of fatigue limit and no fatigue limit in fatigue life prediction of the rolling element are reported in table 2: Effect of fatigue limit τ on rolling-element fatigue life in the paper (24).

2.3.3 Zaretsky Model

The above earlier models relate the critical shear stress-life exponent c to the Weibull slope e . Thus, in essence, the parameter c/e becomes the effective critical shear stress-life exponent, implying that the critical shear stress-life exponent depends on bearing life scatter or dispersion of the data. A search of the literature for a wide variety of materials and non-rolling-element fatigue reveals that most stress-life exponents vary from 6 to 12. The exponent appears to be independent of scatter or dispersion in the data. Hence, Zaretsky (25) has rewritten the Weibull equation to reflect that observation by making the exponent c independent of the Weibull slope e , where

$$f(X) = \tau^{c/e} \eta^e \quad (2.12)$$

From Eqs. (2.11) and (2.12),

$$\eta \sim \left[\frac{1}{\tau} \right]^c \left[\frac{1}{V} \right]^{1/e} \quad (2.13)$$

where η is the number of stress cycles to failure and V is the stressed volume. For critical shearing stress τ , Zaretsky chose the maximum shearing stress, τ_{45} .

Lundberg and Palmgren (9) assumed that once the crack is initiated, the time it takes to propagate to the surface and form a fatigue spall is a function of the depth to the critical shear stress z . Thus, by implication, bearing fatigue Life is “crack propagation time-dependent”. Since rolling-element fatigue life is categorized as “high-cycle fatigue”, Crack propagation time is an extremely small fraction of the total life or running time of the bearing. But the Lundberg-Palmgren relation implies the opposite.

To sort this out i.e to decouple the dependence of bearing life on crack propagation rate, Zaretsky [(25), (26)] dispensed with the Lundberg-Palmgren relation of $L \sim z^{h/e}$ in Eq. (0.4). (Keeping in mind that at the time (1947) Lundberg and Palmgren published their theory (9), the concepts of “high-cycle” and “low-cycle” fatigue were only then beginning to be formulated.)

$L \sim z^{h/e}$ in equation (2.13) gives

$$\eta \sim \left[\frac{1}{\tau}\right]^c \left[\frac{1}{V}\right]^{1/e} \sim \frac{1}{S_{max}^n} \quad (2.14)$$

solving for the value of the Hertz stress-life exponent n , for point contact the above Equation gives

$$n = c + \frac{2}{e} \quad (2.15)$$

where c is calculated by Lundberg and Palmgren to be, for ball bearing, equal to 10.33; e is the slope in the Weibull distribution, equal to 0.60.

Unlike Ioannides-Harris, who used Von Mises criterium to determine the fatigue limiting shear stress τ_u , Zaretsky chose the maximum shear stress.

Ball Set Life

Lundberg and Palmgren (9) did not directly calculate the life of the rolling element (ball or roller) set of the bearing. However, through benchmarking of the equations with bearing life data by use of a material-geometry factor f_{cm} , the life of the rolling-element set is implicitly included in the life calculation.

Failure of the rolling elements in determining bearing life was not initially considered by Palmgren. However, the fraction of failures due to the failure of a bearing component is expressed by Johnson [24] as

$$\textit{Fraction of rolling element failure} = \left[\frac{L_{10}}{L_{re}} \right]^e \quad (2.16)$$

Ball-Race Conformity Effects

The effect of race conformity on ball set life independent of race life is not incorporated into the Lundberg-Palmgren model. An analysis by Zaretsky, Poplawski, and Root [(23) (27)] considered the life of the ball set independently from race life, resulting in different life relations for deep groove and angular contact ball bearings.

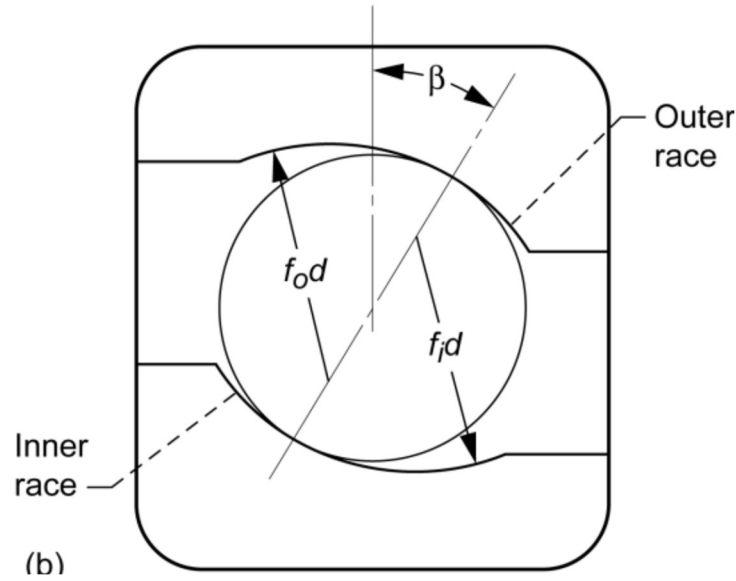


Fig 2 Ball-race conformity in Angular-contact ball bearing.

The conformities at the inner and outer races affect the resultant Hertz stresses and the lives of their respective raceways. The determination of life factors LF_i and LF_o based on the conformities at the inner and outer races, respectively, can be calculated by normalizing the equations for Hertz stress for the inner and outer races to the conformity of 0.52 (the value of 0.52 was chosen as a typical reference value). Stresses are evaluated for the same race diameter as a function of conformity.

The ratio of the stress at a 0.52 conformity to the value at the same normal load P_N at another ball-race conformity, where $n = 9$ or 12 , gives the appropriate life factor

$$LF = \left[\frac{S_{max0.52}}{S_{max}} \right]^n \quad (2.17)$$

where S_{max} is the maximum contact stress (from Hertz theory) and n is the Hertz stress life exponent

for the inner race,

$$LF_i = \left[\frac{\left(\frac{2}{d_e - d} + \frac{4}{d} - \frac{1}{0.52d} \right)^{2/3} (\mu \nu)_i}{\left(\frac{2}{d_e - d} + \frac{4}{d} - \frac{1}{f_i d} \right)^{2/3} (\mu \nu)_{0.52}} \right]^n \quad (2.18)$$

and the outer race,

$$LF_o = \left[\frac{\left(-\frac{2}{d_e - d} + \frac{4}{d} - \frac{1}{0.52d} \right)^{2/3} (\mu \nu)_o}{\left(-\frac{2}{d_e - d} + \frac{4}{d} - \frac{1}{f_o d} \right)^{2/3} (\mu \nu)_{0.52}} \right]^n \quad (2.19)$$

The values of $(\mu\nu)_{0.52}$ are different for the inner and outer races. For various ball bearing series, values of these life factors for conformities range from 0.505 to 0.570, subject to round-off error.

From Hertz's contact theory, the dimensions of the pressure area are given in terms of transcendental functions μ and ν . The values of the product of the transcendental functions $(\mu\nu)$ are tabulated in Table 4. Effect of race conformity and Hertz stress-life exponent n on ball-bearing life as a function of ball bearing series in (24). The product is the function of ball bearing envelope size (S) and they are different for the inner and outer races. The envelope size is:

$$S = \frac{d \cos \varphi}{d_e} \quad (2.20)$$

From Zaretsky's Rule for ball bearings, the life of the rolling element set is equal to or greater than the life of the inner race but less than that of the outer race with $L_{re} = L_i$ and $X = L_o/L_i$. Life Equation can be written as follows:

$$L_{10} = \left[\frac{X^e L_i^e}{2 X^e + 1} \right]^{1/e} \quad (2.21)$$

Applying life factors based on the effect of conformity on the respective lives of the inner and outer races equation (2.21) becomes

$$L_{10_m} = \frac{(LF_i) (LF_o) X L_i}{[2 (LF_o)^e X^e + (LF_i)^e]^{1/e}} \quad (2.22)$$

Dividing the above two equations 2.21 and 2.22 solves for the bearing life factor LF_C . For the ball bearing recognizing conformity LF_C is formulated as

$$LF_C = \left[\frac{(LF_i)^e (LF_o)^e (2 X + 1)}{2 (LF_o)^e X^e + (LF_i)^e} \right]^{1/e} \quad (2.23)$$

Finally, the equation (2.10) can be modified to include the correction LF_C to account for ball-race conformity in Hertzian contact for the estimation of L_{10} bearing system life according to the ANSI/ABMA and ISO life calculations.

$$L_{10} = LF_C \left(\frac{C_D}{P_{eq}} \right)^p \quad (2.24)$$

The bearing fatigue lives in the actual application will usually be equal to or greater than those calculated using the above eq (2.24) which is according to ANSI/ABMA and ISO standards that incorporate the Lundberg-Palmgren model.

For angular contact ball bearings, as we have already derived, the life factor LF_C depends on several factors, including statistical parameters (obtained from Weibull distribution) and specific parameters LF_i and LF_o describing the ball-race conformity effects at the inner and outer races (24).

The above formulation of equation. (2.24) is further extended in the current Thesis to include the Precessional Slip and Micro Inclusion effect for predicting the fatigue life of the bearing rolling element.

Chapter 3

Ball Motions and Precessional Slip Model

Generally, the life models developed to estimate the life of any component are validated by comparing fatigue tests under different loading conditions. Often, introducing correction parameters becomes a necessity to account for various working conditions. For instance, in components like bearings, the correction factors require a complex definition to account for all possible effects of working conditions such as temperature, rotational speed, and lubrication, etc. It becomes even more complex, in the case of bearing rolling element (ball). Case in point, during rotation the contact point on the races remains the same but changes for the ball, mainly because of Spin and Precession.

To achieve the goal of this thesis, which is to develop an Integrated life estimation model with a dedicated Numerical Solver to estimate the fatigue life of the bearing rolling element (ball) under the influence of the Precessional Slip in the presence of micro-inclusions. The bearing life model (discussed in the previous chapter) had to be modified, to consider the

ball's spin and precession motion during shaft rotation, to estimate the actual contacts occurring between the race and the point of the ball surface below which the microinclusion is present.

The nature of the frictional forces and moments applied to an angular contact bearing rolling element (ball) are examined in terms of slip, spin, and precession. Experimental methods for determining these quantities are given in (28) together with results, that indicate that the ball is retainer-controlled for pivoting and race-controlled for slip. Slip here is defined as the vector difference in surface velocities between the ball and any contacting body. Pivoting often referred to as "spin" is defined as that component of the relative angular velocity of two bodies in contact which is perpendicular to their plane of tangency. The spin is vital in the discussion of the ball's precessional motion.

The Precession motion of the ball is defined as the change in the orientation of the rotational axis of the ball. In an appropriate reference frame, it can be defined as a change in the first Euler angle, whereas the third Euler angle defines the rotation itself. Analysis with formal calculations on explicit forms of ball-race slips with and without precession are provided in (29).

In this chapter Conditions leading to Precession and definition of Precessional EHD slip fields are investigated for a clear understanding of precessional slips. A model is developed for the estimation of precessional slip at the ball-race contacts in a Ball Bearing SKF BAHB-311396B.

3.1 Precessional Slip

Ball precessional motion in an angular contact bearing is analyzed (29). It was shown that the *observed precession does not change the Hertzian slip fields* very much at either contact, compared with those produced by pure spin.

Various theoretical slip fields have been proposed for the Hertz areas in an angular contact ball bearing to account for the fact that “pure rolling contact” or “roll without slip” is impossible. Heathcote slip (30) and pivoting slip or often loosely called spinning slip (31) are examples of kinematic theories. Gyroscopic slip (32) is a dynamical theory and micro slip (33) is for an elastic contact with traction. These theories assume dry friction and predict points, lines, or zones of zero slip (“lock-up”) inside the Hertz area.

All these theoretical or traditional bearing slip analyses are gradually undermined by the development of Elastohydrodynamic (EHD) theory. Also, No convincing experimental demonstration of any of those aforementioned slip theories has been forthcoming for a real ball bearing. For example, in Kingsbury (34) K. C. Falcon and C. Andrew questioned the use of race control theory based on dry friction pivoting slip for the analysis of a lubricated bearing. And Poritsky (35) questioned whether the shearing of the lubricant renders the previous theory of micro slip completely inapplicable considering ball bearing.

For a lubricating bearing, an Elastohydrodynamic slip field is reported, derived from kinematic measurements (36) in the support of those comments. Results are interpreted as drug-induced shear within the EHD film, and a uniform slip field *of about 1% of surface velocity* in the circumferential direction over the whole Hertz area.

In addition to the EHD slip field, the possibility of the presence of a second slip field in a lubricated bearing follows from the experimental observation of ball precession [(37) (38)]. In this motion, the ball spins at rate s about the axis of the figure, which simultaneously cones or precesses at a rate p about an “invariable line”. s and p are oblique components of the ball angular velocity vector δ^{\bullet} and include the precession angle θ .

Figure 1, taken from ref. (28), shows stroboscopic photographs of a precessing ball. The ball has been given a through-hole to establish its axis of the figure, and a fiduciary mark to aid in rate measurement. The bearing is in the “counter-race rotation mode” for stationary ball centers. s, p, δ^{\bullet} , and θ can all be determined from Fig. 3.

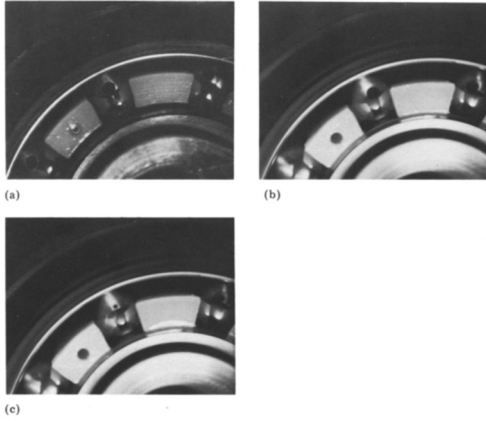


Fig 3 Ball Precession:

(a) bearing stationary ;(b) ball center stationary, ball precessing, stroboscopically illustrated at p ; (c) ball center stationary, ball precessing, stroboscopically illuminated at $\delta^{\bullet} = | \mathbf{p} + \mathbf{s} |$

Apart from pure spin obtained during ordinary operations, Precession requires different slips in ball-race contacts. Defining a Precessional EHD slip field and the conditions leading to Precession are investigated to provide a clear understanding of Precessional slips.

In this thesis, a model is developed for the estimation of precessional slip at the ball-race contacts in the Ball Bearing SKF BAHB-311396B (Ball material: 100Cr6). The calculations use an Eulerian reference system to

describe precession and are for the counter-race rotation mode with zero ball orbit rate.

3.2 Ball Local Reference Frame

A fixed reference frame ($O'X'Y'Z'$) with unit vectors i', j', k' has $O'X'$ along the bearing axis and $O'Z'$ through the center of the ball ($n = 1$) Fig. 5 for a full complement retainer less bearing (29).

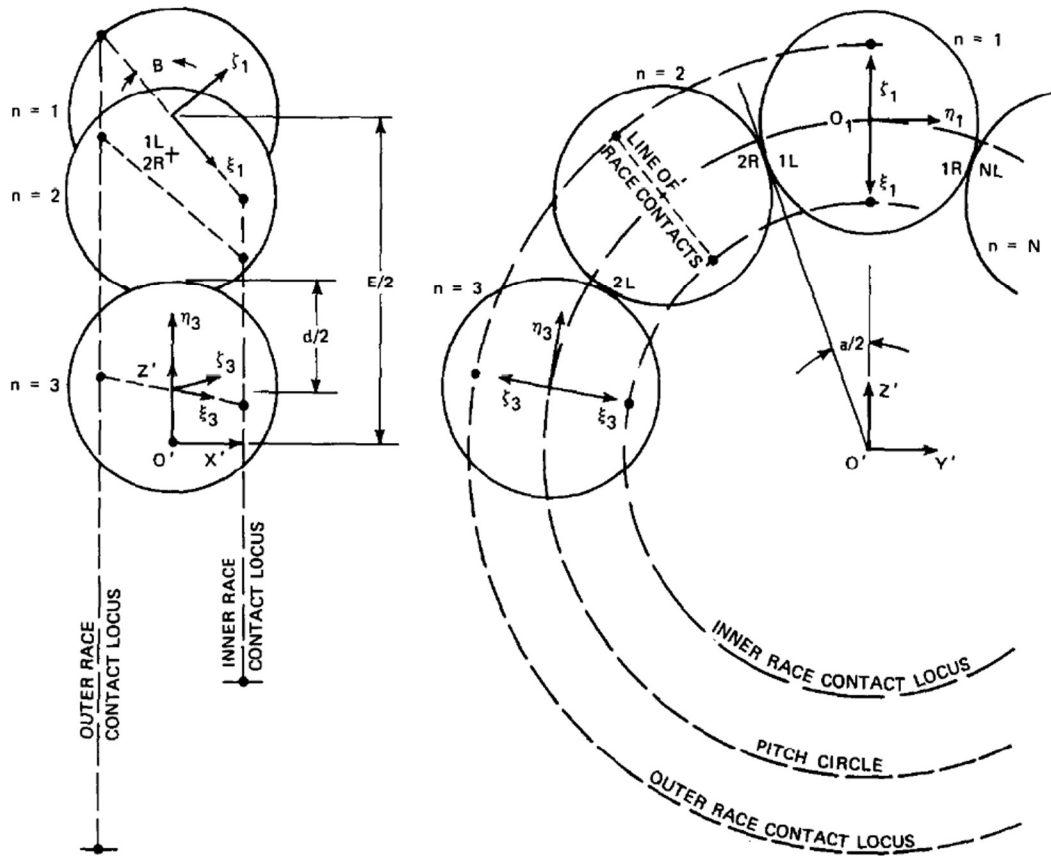


Fig 4 Contact Geometry

The spacing angle α is the angle between adjacent ball centers and the angle $(n-1)\alpha$ for $(n = 1, 2, \dots, N)$, measured around the pitch circle from $O'Z'$, locates the center of the n^{th} ball.

A series of fixed frames $(O, \xi, \eta, \zeta)_n$ having unit vectors $(i, j, k)_n$ is centered one on each ball, each frame obtained from $(O'X'Y'Z')$ by (30) rotation about $O'X'$ through $(n - 1)\alpha$ and (31) rotation about the new position of $O'Y_n$, through $\left(\frac{\pi}{2} - B\right)$.

Thus, at each ball, i_n is normal to the Hertz contact area, j_n is in the rolling direction and, k_n is across the roiling direction Fig. 5. $(i, j, k)_n$ are given in terms of (i', j', k') in $(O'X'Y'Z')$ by (29)

$$\begin{aligned} i_n &= i' \sin B + j' \sin\{(n - 1) \alpha\} \cos B - k' \{\cos (n - 1) \alpha\} \cos B \\ j_n &= j' \cos \{ (n - 1) \alpha \} + k' \sin\{ (n - 1) \alpha \} \\ k_n &= i' \cos B - j' \sin\{(n - 1) \alpha\} \sin B + k' \{\cos (n - 1) \alpha\} \sin B \end{aligned} \quad (3. 1)$$

For any typical Bearing, these vectors should be close to 1.

This reference system is modeled for full complement retainer less angular contact bearing (29). But in our experimental setup, a cage or retainer was introduced to limit the deviation of the rolling element from its mean position to avoid any random slip. Also, our experimental setup was modeled to focus the failure on the rolling element (ball). This was done by modifying the bearing by removing some balls. Due to the lack of experimental data, the same reference system can be assumed for our case as well.

3.3 Ball Angular Velocity with Precession

The precessional angular velocity of the ball is obtained by boring a small hole through its center. Under ordinary conditions, the hole axis establishes itself as the rotation axis for the ball, whose rate is then easily measured. To facilitate the precession of the bored balls, 200 cP mineral oil was replaced with n-hexadecane (37). It was found that bored balls may precess.

For any ball precessing in counter-rotation, its angular velocity vector δ'_n is made up of two oblique components. Spin s along the hole axis and precession p of the hole axis. These include the precession angle θ , which is constant for zero nutation (the case considered here) (Fig. 5).

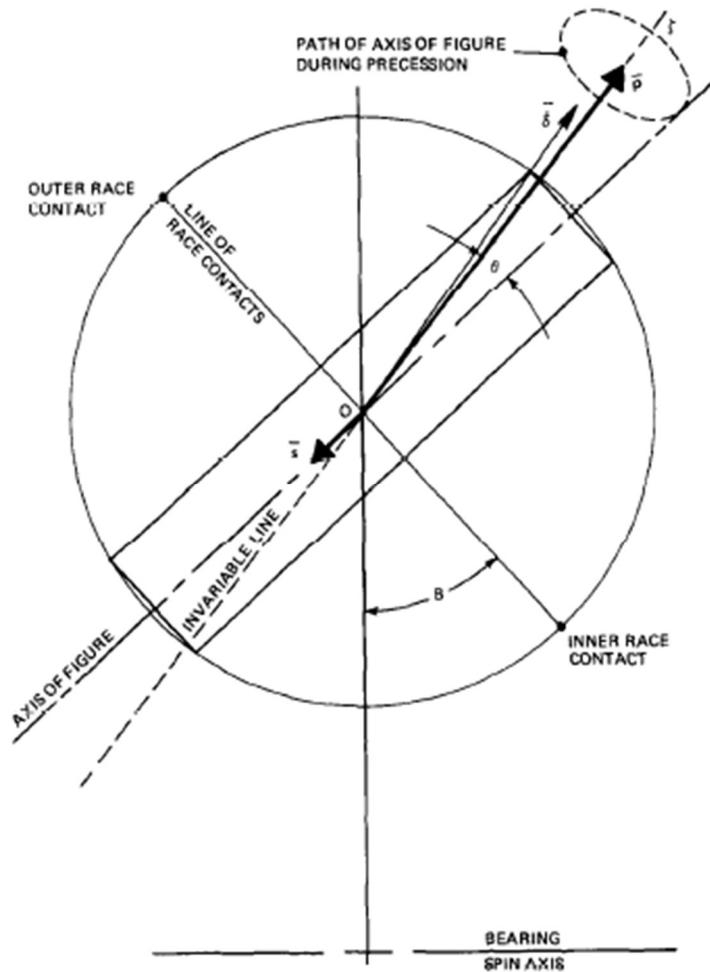


Fig 5 Precession Geometry

When 200 cP oil was added to the precessing bearing, the precession stopped instantly. Photographs of a typical precession have been taken under stroboscopic illumination (37) to illustrate this effect. Figure 6 shows the bearing not running for comparison. The bored balls are marked with a line to aid in measuring angular displacements.

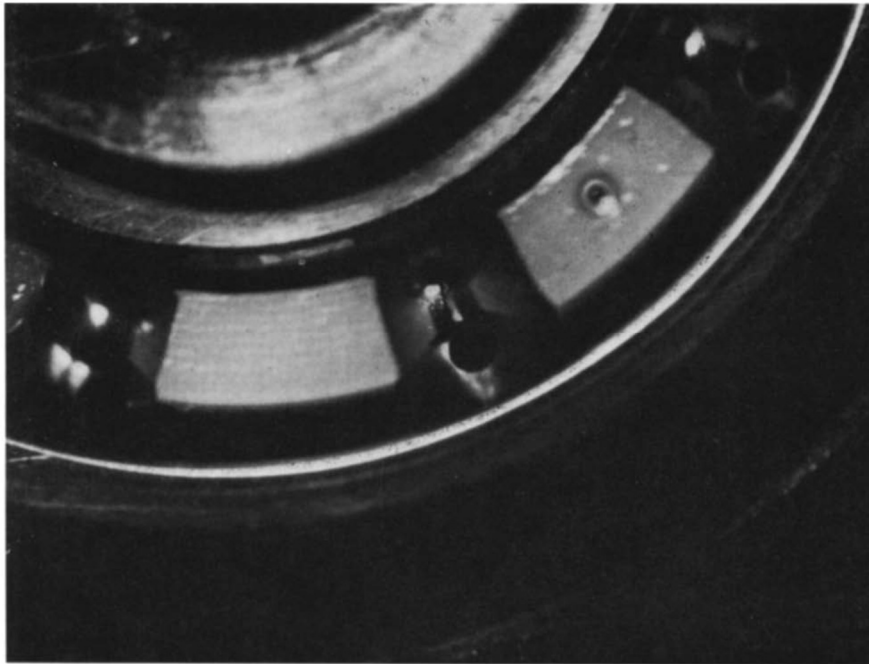


Fig 6 Bearing not running

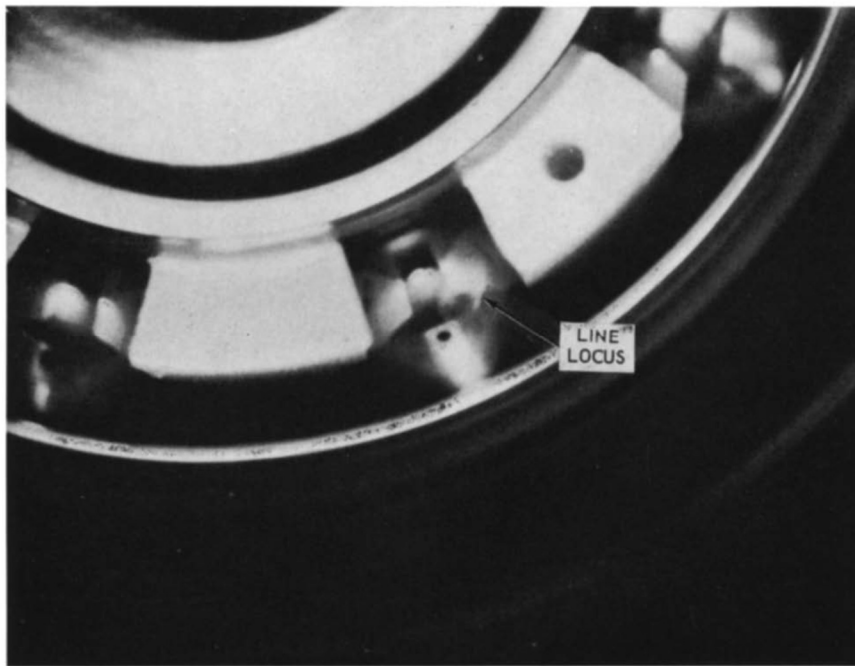


Fig 7 Bearing counter-rotating with ball precession, illuminated at δ°

Figure 7 shows the bearing counter-rotating at 9000 rev./min with precession. Illumination is provided by the stroboscope set at the ball angular velocity frequency δ^\bullet . The locus of the line can be made out above and to the right of the hole overlap.

This pattern represents all the possible positions of the line at those times when it is parallel to some arbitrary direction and is characteristic of the total angular velocity. Figure 6 is the same except that the stroboscope frequency is set equal to the precession rate δ . The line is not resolved since it is masked by the spin rate s ; however, the hole true diameter is now visible.

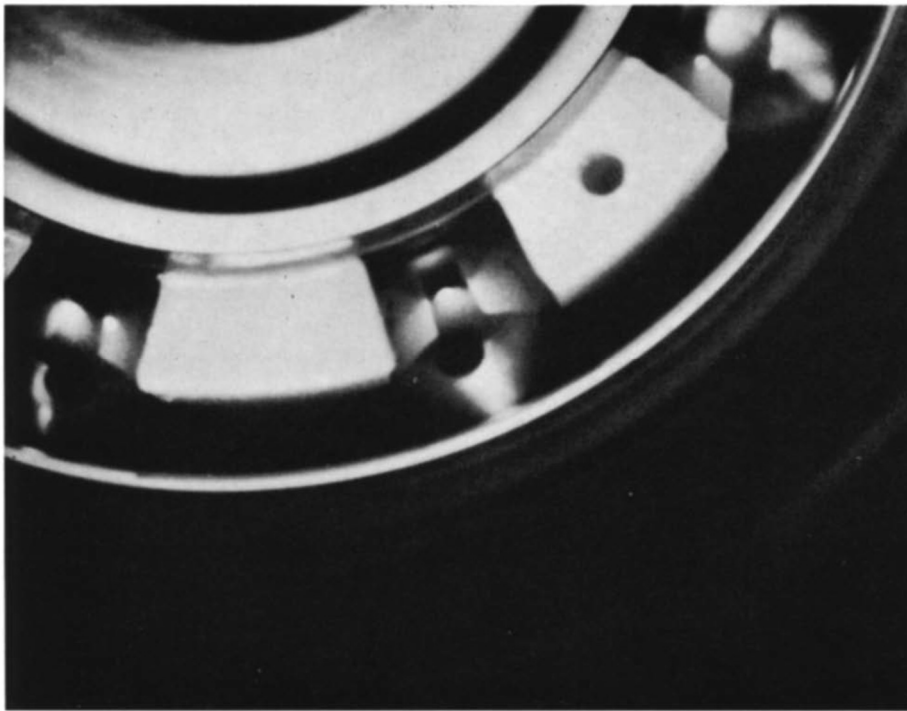


Fig 8 Bearing counter-rotating with ball precession, illuminated at p

The bored balls are rigid bodies having an “axis of the figure” (the hole axis) in motion about a fixed point (the ball center for counter-rotation). Recognizing the classical definition of a gyroscope, obeying Euler’s

equations, two solutions of these equations exist for the case when external moments on the ball are zero. The first corresponds to a simple rotation of the ball about an axis fixed in space. The second solution describes the “Poinsot” precession of the ball and requires that the spin and precessional components of the ball angular velocity be related according to

$$\frac{I_E}{I_E - I_H} \cdot s = p \cos \theta \quad (3.2)$$

But

$$p^2 + s^2 + 2 ps \cos \theta = \delta^2 \quad (3.3)$$

p and θ may be obtained separately through the stroboscope; θ may be estimated from a photograph ($\cos \theta$ approximates to 1 for $0 > \theta > 10^\circ$ in any case), $\frac{I_E - I_H}{I_E}$ is easily calculated according to the ball and hole diameters; thus a check of Eqn. (3.2) is possible, with the result that the observed precession corresponds to the “Poinsot” case to a few percent.

The Ball Angular Velocity with Precession motion is specified for fixed reference frame $(O, \xi, \eta, \zeta)_n$ as a function of time t by

$$\delta \bullet_n = (s \sin \theta \cos pt) i_n + (s \sin \theta \sin pt) j_n + (p + s \cos \theta) k_n \quad (3.4)$$

By solving the expression from Eqn. (3.2) and Eqn. (3.3) with respect to our experimental conditions, the values of spin and precession can be estimated. Our calculations show spin vector value negative, which means that Spin and Precession point more or less in opposite directions, and Precession is Retrograde.

3.4 Ball-race contact velocity

The surface velocities of the ball and race at both inner and outer contact are determined (29). For the ball with $n = 1$, the radius vector to the ball-outer (ball-inner) contact is

$$r_{Bo(i)} = \pm \frac{d}{2} i_1 \quad (3.5)$$

The surface velocities on the ball at these contacts are

$$V_{Bo(i)} = \delta^\bullet \times r_{Bo(i)} = \frac{d}{2} [\pm(p + s \cos \theta) j_1 \pm (s \sin \theta \sin pt) k_1] \quad (3.6)$$

In frame $(O, \xi, \eta, \zeta)_1$ the inner and outer race angular velocities are

$$\gamma^\bullet_{o(i)} = \gamma^\bullet_{o(i)} (\pm \sin B i_1 \pm \cos B k_1) \quad (3.7)$$

where $\gamma^\bullet_{o(i)}$ is the magnitude of race angular velocity vector $\boldsymbol{\gamma}^\bullet_{o(i)}$.

The radius vectors from O' to the ball-race contacts are

$$r_{o(i)} = \frac{1}{2} (E \pm d \cos B)(-\cos B i_1 - \sin B k_1) \quad (3.8)$$

and the surface velocities on the races are

$$V_{o(i)} = \boldsymbol{\gamma}^\bullet_{o(i)} \times r_{o(i)} = -\frac{1}{2} \gamma^\bullet_{o(i)} (E \pm d \cos B) j_1 \quad (3.9)$$

3.5 Ball-Race Slips

The slip velocities at ball-race contact in the presence of precession and spin velocities in ordinary conditions (pure spin) are estimated. The ball-race slips, defined as race minus ball surface velocity, are

$$\begin{aligned} V_{s(o)} &= \frac{1}{2} \left\{ d(p + s \cos \theta) - (E + d \cos B) \gamma_{(o)}^\bullet \right\} j_1 - \frac{1}{2} \{ s \sin \theta \sin pt \} k_1 \\ V_{s(i)} &= \frac{1}{2} \left\{ d(p + s \cos \theta) - (E - d \cos B) \gamma_{(i)}^\bullet \right\} j_1 + \frac{1}{2} \{ s \sin \theta \sin pt \} k_1 \end{aligned} \quad (3.10)$$

For pure spin, $p = \theta = 0$, $\delta^\bullet = s$, and

$$\begin{aligned} 2V_{s(o)} &= \left\{ \delta^\bullet d - (E + d \cos B) \gamma_{(o)}^\bullet \right\} j_1 \\ 2V_{s(i)} &= \left\{ \delta^\bullet d - (E - d \cos B) \gamma_{(i)}^\bullet \right\} j_1 \end{aligned} \quad (3.11)$$

The differences between Slip Velocities with and without Precession (pure spin) at Ball-Race contact are compared. Our results show the slip velocities in the case of precession are about one-half to that of pure spin.

3.6 Basic Speed Ratio with Precession

In Angular Contact Ball Bearing, the ratio of Ball Angular Velocity (δ^\bullet) and Total Speed of the Bearing (S) at each ball-race contact in the rolling direction (j_n) gives Basic Speed Ratio. The algebraic difference in race rates $\gamma_{(o)}^\bullet - \gamma_{(i)}^\bullet = S$ is the total speed of the bearing.

The definition of Basic Speed Ratio can be generalized using First-order bearing theory. The first-order bearing theory assumed zero slip in the rolling direction (j_n) at each ball-race contact. Agreeing to this condition (39) (40), solving equation (3.11) gives

$$\rho = \frac{\delta^\bullet}{\gamma^\bullet_{(o)} - \gamma^\bullet_{(i)}} = \frac{\delta^\bullet}{S} = \frac{E^2 - d^2 \cos^2 B}{2Ed} \quad (3.12)$$

Although eqn. (3.12) is derived for the case of counter-rotating races and zero ball orbit rate, it also holds for any other combination of race rotations. The uniform EHD slip field is a correction and refinement introduced to this first-order theory.

Now with precession, eqn. (3.10) shows that zero slip is kinematically impossible, even to first order. However, zero circumferential slip is still possible with the presence of a precession and spin vector along with a precession angle. Thus, considering zero circumferential slip, with precession, the definition of basic speed ratio can be generalized to (29)

$$\rho_p = \frac{p + s \cos \theta}{S} = \frac{E^2 - d^2 \cos^2 B}{2Ed} \quad (3.13)$$

3.7 Spin-Precession Ratio

The influence of the oblique components: spin and precession on the ball angular velocity can be analyzed by determining the spin-precession ratio. For a free or Poincot precession (i.e., if the net external moment on the ball is close to zero) p , s and θ are related to the spin-precession ratio by (29)

$$\frac{s}{p} = \frac{I_E}{I_E - I_H} \cos \theta \quad (3.14)$$

where I_H and I_E are ball inertias along and normal to the axis of the figure. If $\cos \theta = 1$, eqns. (3.13) and (3.14) can be solved for an estimate of s and p . In the experiment of Fig 1 (37), $\frac{I_E}{I_E - I_H} = -0.06$, and $\theta = 10^\circ$. Thus $\frac{s}{p} = -0.05$, showing, that most of the ball surface velocity comes from the precessional component of angular velocity. In the absence of the

precession component i.e., pure spin, all surface velocities must of course come from spin. Since $I_H > I_E$, spin and precession point more or less in opposite directions and the precession is “retrograde”.

3.8 Transverse Precessional Slip

For the precessional motion to occur, Ball Precession requires a time-varying transverse precessional slip field at outer and inner ball-race contact. In other words, Transverse Precessional Slips must form at both inner and outer ball-race contact across the rolling direction for the precessional motion to occur.

Transverse precessional slips (in the k_n direction) is given by

$$TPS_{o(i)} = \pm \frac{d}{2} \{s \sin \theta \sin pt\} \quad (3.15)$$

at the outer (inner) ball-race contacts. They are equal, opposite, and sinusoidal at the precession rate. Thus, ball precession requires a time-varying transverse slip field at each ball-race contact. For small s compared with d and small θ (the case in Fig.3) (37), the magnitude of the transverse slip is small.

Slip, Entrainment, and Contact velocities at Ball-Ball contact are determined for Retainerless Ball Bearing in (29). The bearing used in our experimental setup is the Angular Contact Retainer Bearing. The balls were separated using a cage or retainer. Thus, Calculations on contact, slip, and entrainment velocities at Ball-Ball contact can easily be neglected.

3.9 Ball Spin Frequency

When a bearing spins, any defect or irregularities such as indentation, spall, crack, flaking in the roundness of the rolling element (ball) or the raceway

surfaces excites periodic frequencies called fundamental defect frequencies. A machine with a defective bearing can generate at least five frequencies (41). The frequencies are:

- Rotating unit frequency - ball frequency
- Fundamental Train Frequency - cage frequency
- Ball Pass Frequency of Outer race - race frequency
- Ball Pass Frequency of Inner race - race frequency
- Ball Spin Frequency - circular frequency of each rolling element it spins.

Neglecting the cage and race frequencies, as our model focus only on the rolling element. By the definition of the BSF, for every revolution of the rolling element (ball) the defect such as spall hits once both to outer and inner race simultaneously.

To statistically determine how often the inclusion (defect) is loaded i.e the frequency with which the surface point near the inclusion contacts outer and inner race, the following BSF formulation (42) for a bearing is given

$$BSF = \frac{E}{2d} \left(1 - \left(\frac{d}{E} \cos B \right)^2 \right) \quad (3.16)$$

where BSF is the Ball Spin Frequency, E is the bearing pitch diameter, d the bearing ball diameter, and B is the contact angle. The contact angle is defined as the angle between the line joining the points of contact of the ball and the raceways in the radial plane (along which the combined load is transmitted from the raceways), and the line perpendicular to the bearing axis. It must be noted that a fault in the ball strikes twice this frequency, once the inner race and once the outer race.

BSF estimate the total number of cycles in which a ball rotates during a complete shaft cycle, assuming no slip. Since rolling without slip is

impossible, some slip is present, and it is damaging (2). Furthermore, the angle B varies with the position of each rolling element in the bearing as the ratio of local radial to axial load changes. Then each rolling element has a different (in direction) effective rolling diameter and each ball tends to rotate at a different speed. The cage limits the deviation of the rolling elements from their mean position, thus causing some random slip. Thus, becomes necessary to consider the transverse slip (eqn. (3.15)).

3.10 Transverse Slip Ratio

The amount of slip a ball undergoes and how it is linked to the complete revolution of the ball in one shaft cycle is given by the ratio of transverse slip amplitude to ball surface velocity in the motion eqn. (3.16). This ratio of transverse slip done by the ball while doing a complete rotation around the principal axis is modeled by the following formula (29) for ball-race contact, in presence of retainers as per our experimental condition.

$$R = \frac{\text{tranverse slip amplitude}}{\text{ball surface velocity}} = \frac{s \sin \theta}{p + s \cos \theta} \approx \frac{1}{100} \quad (3.17)$$

i.e transverse slip is about 1% of ball surface velocity. Our developed mathematical model solver (discussed in later chapters), subjected to experimental bearing parameters (SKF BAHB-311396 B) validates this condition. The ratio obtained was 0.023 which is about $\frac{2}{100}$ i.e While Ball did one complete cycle around the principal axis, at the same time also did a transverse slip of about 2/100th of a complete cycle.

In support of the comments on the EHD slip field already discussed in section 3.1 of this chapter, both transverse and circumferential slip fields at ball-race contacts are Lubricant Shear Phenomena. They differ from traditional slip fields. Neither of them predicts lock-up in the Hertz zone as suggested by the experimental observation (29). Uniform slip field is about

1% of the surface velocity in circumferential direction over the whole Hertz area.

Similar experiments in pure spin (36) showed Circumferential slip was also about 1% of surface velocity. Both slip fields may be present in a Precessing bearing: a time-varying transverse slip superimposed on a uniform drug-induced circumferential slip. A maximum EHD pivoting slip of the same order can also be calculated (assuming no race control) for this contact. All three slip fields may be involved in a shear-activated lubricant degradation process (43) (44).

This sudden onset of precession might seem a large and violent change from an existing pure spin. Interestingly, the required additional precessional slips are of the same order as preexisting drag slips (29). However, most of the ball surface velocity changes from a rotation about an axis (spin) to a conical motion of the axis (precession). The spin component of angular velocity suffers an order-of-magnitude diminution and an almost complete reversal in direction, yet the slip velocities are not much changed at ball-race contact.

3.11 Inclusion Loading Frequency

Assuming that the transverse slip is not random, but always in the same direction of rotation, Micro-inclusion loading frequency. i.e., how frequently the inclusion in the ball contacts the raceways can be determined using the inverse of the transverse slip ratio.

$$\frac{1}{R} = \frac{\text{Shaft revolution}}{\text{transverse slip}} \quad (3.18)$$

Considering that the inclusion is loaded twice during a complete rotation (once with inner race and once with outer race), the actual micro-inclusion loading frequency would be once half of $\frac{1}{R}$ shaft revolutions. It is

furthermore assumed that the load is effective on damaging the rolling element only if the contact occurs when the microinclusion is exactly below the contact point.

Chapter 4

Non-Metallic Inclusions

Non-metallic inclusions (NMIs) are chemical compounds and non-metals that instigate many important properties of steel and other alloys, influencing both the processing and application of components such as bearings. They are the product of chemical reactions, physical effects, and contamination that occurs during the melting and pouring process.

For two bodies in contact (in our case: bearing ball and raceway), the superficial and sub-superficial stress distribution is estimated by Hertz's theory. If NMIs are present in any of these contacting bodies, specifically near the surface of either contacting body, they lead to Rolling Contact Fatigue. As we have already discussed, RCF predominantly involves Sub-Surface Spalling, and spalling is the main cause of failure in bearings.

Spalling, in its early stages, is manifested by the development of cracks and an accompanying characteristic microstructure alteration called “Butterflies” around the micro-structural inhomogeneities such as non-metallic inclusions (NMIs) located in the sub-surface region. That is to say, Spalls typically appear near the NMIs, where the hertz contact shear stress

reaches the maximum. NMIs act as stress risers facilitating crack nucleation, propagation, and eventually failure.

Eshelby's Microinclusion Model (45) is widely used in literature to quantify the stress increase inside the inhomogeneity. A coupled damaged model solver (3) simulates the butterfly wing formation around the microinclusion. By superimposing inclusion's stress and strain field, the interactions between multiple inclusions (pairs, clusters, and stringers) were investigated (7). This study presents an investigation on the influence of microinclusions on the fatigue performance of bearing rolling element (steel alloy 100Cr6).

This steel alloy is defined in international Standards as UNI 3097 and DIN 17230 as 100Cr6, AISI/SAE as 52100, AFNOR 35-565 as 100C6. Many researches have dedicated this steel for experimental and numerical approaches. In (50) and (4), an empirical approach of Linear Elastic Fracture Mechanics (LEFM) is used to analyze the high sensitivity of high resistance steels to microinclusions and defects. The fatigue limit was found to be about 850 MPa. The Eshelby model allows computation of the stress field inside an ellipsoidal inclusion. The stress within the ellipsoidal inclusion is uniform if the embedded matrix is subject to a uniform load. Meaning, the elastic stress, and strain do not change inside the inclusion.

The effect of NMIs on the fatigue life of the component based on its size, shape, location, and composition is already described in many experimental, analytical, and numerical studies (46) (47). Of all of them, RCF is mainly influenced by the dimension of the largest inclusion present in the material. NMIs can be controlled with improved steel cleanliness. However, they cannot be completely eliminated in steelmaking.

As mentioned before, this thesis aims to estimate the bearing life considering the stress increment due to sub-superficial microinclusions in

rolling balls under the influence of the Precessional Slip. In the evaluation of the micro-inclusion effect on stresses, the Eshelby-Mura model was applied to estimate the stress field surrounding a single microinclusion and the Moschovidis model to take into account the effect of the interaction of microinclusions on stress. The models were applied to the failed specimens of the experimental campaigns. Experimental failures provided microinclusions composition, shape, aspect ratio, geometry, and location. Then, stresses with precessional slip effect were evaluated and fatigue life was estimated. The predicted and actual fatigue life were then compared to validate our model.

4.1 Types of Inclusions

Based on similarities in morphology (48), Non-metallic inclusions are divided into four macro-categories:

- Sulfides
- Aluminates
- Silicates
- Oxides

For different inclusion types, respective thermal and mechanical properties are tabulated (Table 2) taken from Brooksbank, 1970. Hard inclusions with low deformability are the most dangerous. They cause microcrack formation at the interface between the inclusion and the matrix during the steel-making process. Fatigue cracks initiate from these microcracks.

Table 1 Values of coefficients of thermal expansion α , Young's modulus E, and Poisson's ratio ν

Inclusion type	Inclusion	$\alpha \times 10^{-6}/^{\circ}\text{C}$ (0 ~ 800 °C)	E (GPa)	ν
Sulphides	MnS	18,1	(69-138)	(0,3)
	CaS	14,7		
Calcium aluminates	CaS-6Al ₂ O ₃	8,8	(113)	(0,234)
	CaS-2Al ₂ O ₃	5,0		
	CaO-Al ₂ O ₃	6,5		
	12CaO-7Al ₂ O ₃	7,6		
	3CaO-Al ₂ O ₃	10,0		
Spinel	MgO-Al ₂ O ₃	8,4	271	0,260
	MnO-Al ₂ O ₃	8,0		
	FeO-Al ₂ O ₃	8,6		
Alumina	Al ₂ O ₃	8,0	389	0,250
	Cr ₂ O ₃	7,9		
Nitrides	TiN	9,4	(317)	(0,192)
Oxides	MnO	14,1	(178)	(0,306)
	MgO	13,5	306	0,178
	CaO	13,5	183	0,21
	FeO	14,2		

The study of the rolling contact fatigue of bearing steels concerning various oxide inclusion is reported in (49). Specimens containing Al₂O₃ or Al₂O₃ CaO inclusions showed a lower fatigue life compared to specimens containing SiO₂ Al₂O₃ inclusions. Alluminates consist of angular oxide particles with an aspect ratio of less than 2. They are aligned nearly parallel to the deformation axis (Fig 10). Oxides have a globular shape (Fig 11).

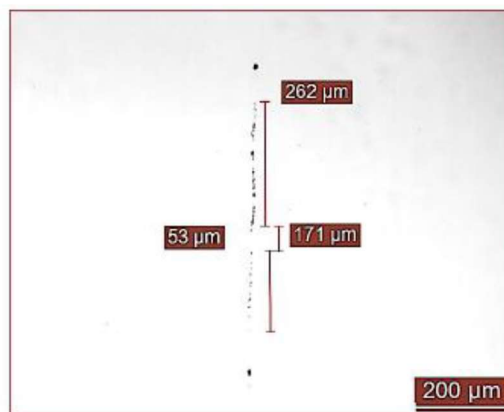
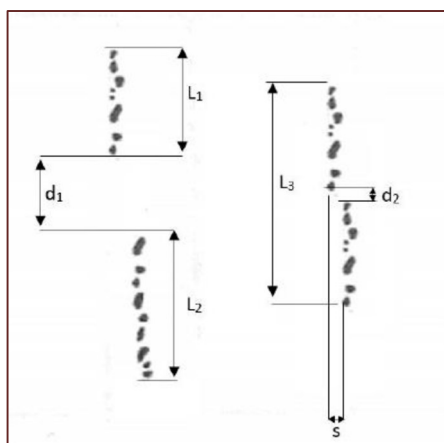


Fig 9 Alluminates type

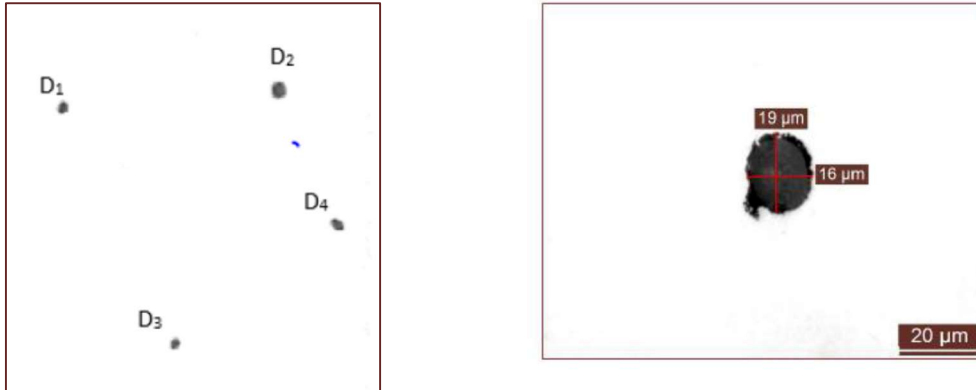


Fig 10 Oxides type

4.2 Factors influencing stress peak

Simulations coming from numerical tests (50) based on the experimental data coming from test rig failures help us understand the characteristics of the inclusions more relevant for stress increase in steel's matrix. It is now well known that inclusions act like a stress raiser. The stress distribution around the micro inclusion is estimated using a dedicated 3D numerical MATLAB solver (50) implementing the Eshelby microinclusion model (45). This model is widely used in literature. Eshelby found was that if the inclusion is ellipsoidal and the matrix in which it is embedded is subjected to a homogeneous load, the stress within the inclusion is uniform i.e the elastic stress and strain do not change with the position of the inclusion.

Different effects of the stress field around the microinclusion are simulated by changing the parameters, taking into account the real found inclusion from experimental tests. The effect of shape, chemical composition, depth, and dimension, on the increase of stress at inclusion's boundary, is detailed in the following sections.

4.2.1 Dimension

Different inclusion sizes (ranging from 8 to 16 μm) were studied. Although inclusion size strongly affects the area of the stress field around the inclusion, there is no significant change in the Tresca stress peak values (table 3). Two samples (Matrix elastic modulus E_m of 210 GPa, Inclusion elastic modulus E_h of 375 GPa, and Depth of 200 μm) with the same position and chemical composition but different inclusion sizes show the same stress levels i.e inclusion size has no strong influence on the stress concentration (Fig 11 and Fig 12) (50).

These results are partially in agreement with Gabelli et al. (51), who found that defects smaller than a threshold do not affect the fatigue life of bearing high-strength steels. According to Moghaddam et al. [12], large inclusions are more critical because statistically, they are more likely to be located at the critical depth when compared to smaller ones. Aluminum oxide inclusions were investigated to study the effect of size, depth, and elastic modulus on stress distribution and crack propagation, using a FEM approach. However, only inclusions larger than a certain critical size can affect fatigue life.

Table 2 Effect of Inclusion dimension

Tresca stress evaluated for different inclusion size	
Semiaxis of inclusion size [μm]	Tresca peak increment
0.5 x 0.5 x 0.5	+39%
50 x 50 x 50	+39%

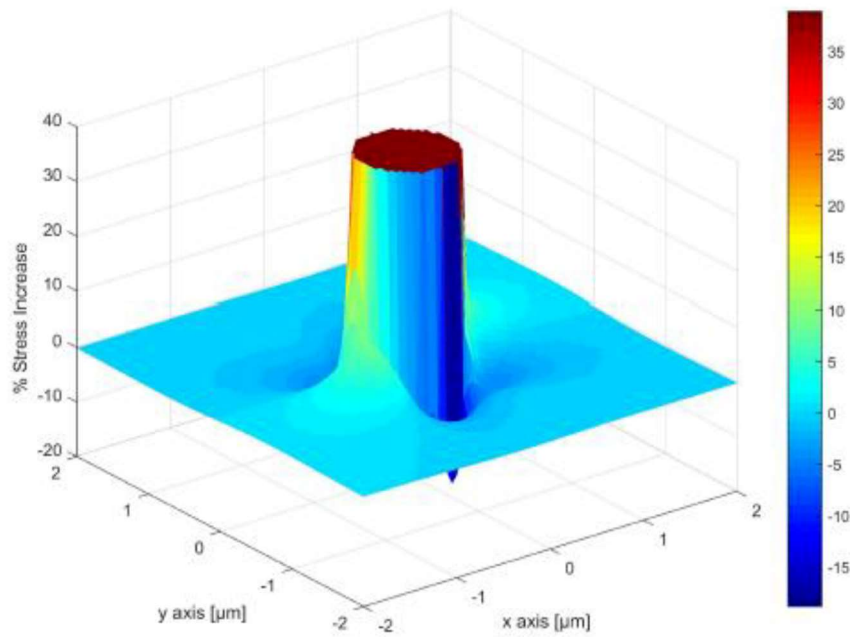


Fig 11 Stress Threshold for inclusion size of 0.5 μm radius

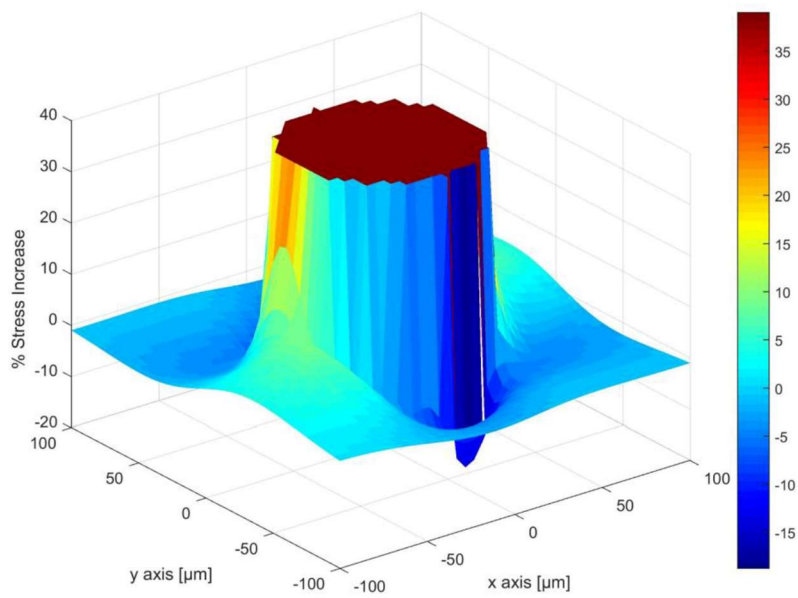


Fig 12 Stress Threshold for inclusion size of 50 μm radius

4.2.2 Depth

The stress peak at the inclusion boundary is influenced by the depth at which the inclusion is located. Also, from hertz theory, the maximum equivalent stress is located at a certain depth (approximately 75% of the contact half-width b) below the surface (47). If the inclusion is far from the surface, it will not be the main reason for spalling (6).

$$Depth_{eq,max} = 0.75 b \quad (4.1)$$

Irrespective of the depth i.e the location of the inclusion below the surface, the percentage stress increment due to the presence of NMIs will remain the same (Table 4) (50). As the steel matrix stress calculated by hertz changes, the absolute increase is maximum at a critical depth (Fig 13).

Table 3 Effect of inclusion depth on stress increment

Stress peak increment at NMI boundary	
Depth [b]	Tresca stress peak Increment
35%	+39%
71%	+39%
175%	+39%

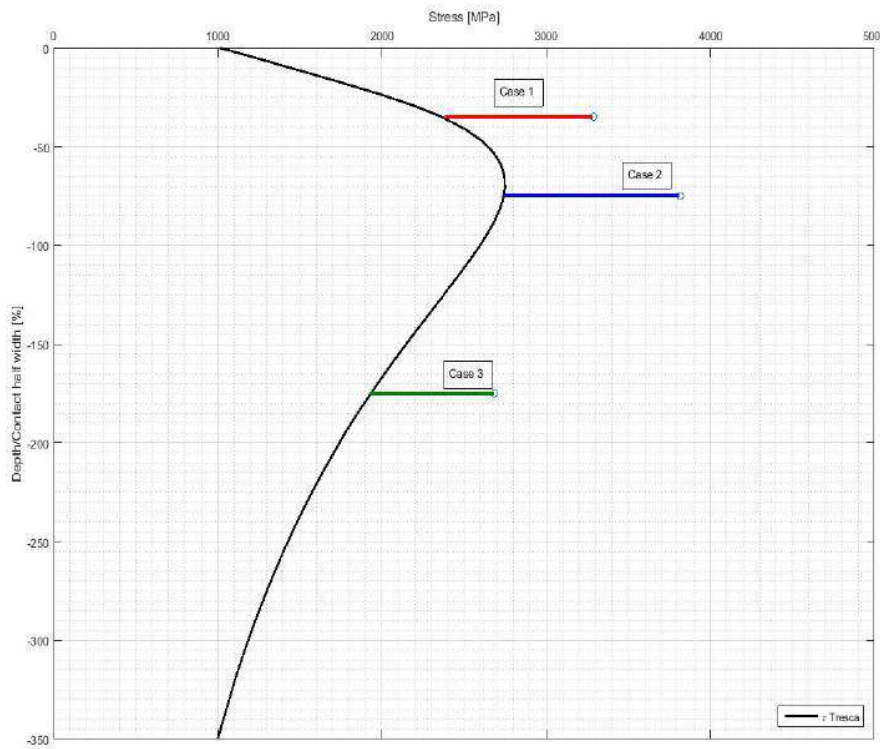


Fig 13 Effect of depth (contact half-width) on Tresca Stress

4.2.3 Shape

The inclusion shape influences the stress peak at the inclusion's boundary. The stress peak significantly increases as the aspect ratio of the two semi-axes of the inclusion increases. Inclusion semi-axes are perpendicular to the direction of the force applied (force applied along the z -axis). The effect of the inclusion's Aspect Ratio on the increase of the equivalent Tresca stress (Al_2O_3 in 100Cr6 matrix, located at $z = -453 \mu\text{m}$) is shown in Fig 14 (52).

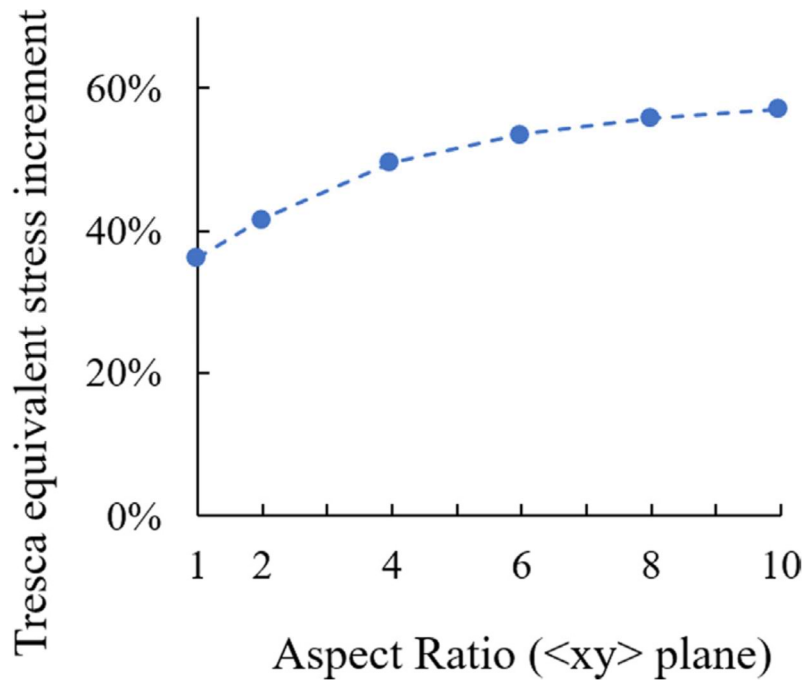
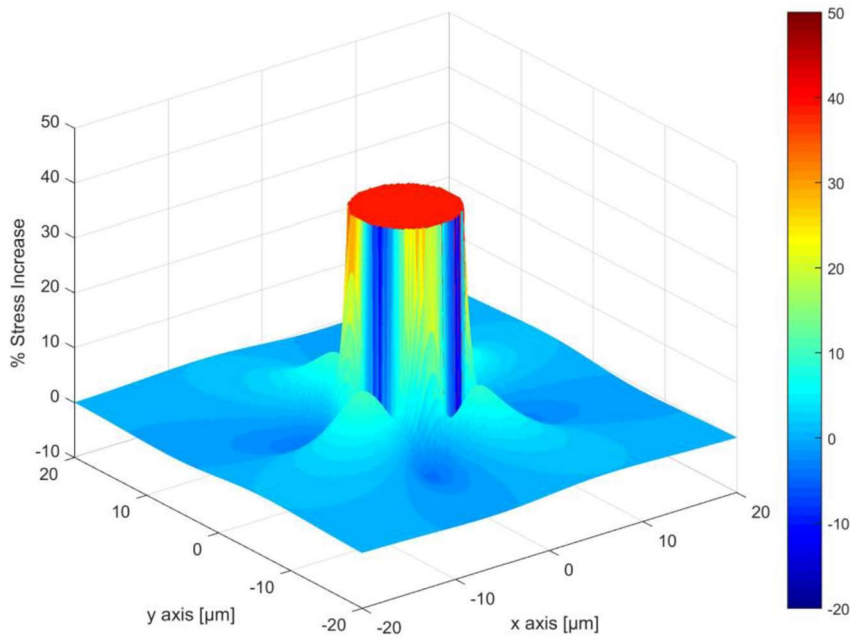


Fig 14 Influence of Aspect ratio (y/x) on stress peak

The larger is the difference in the length of the semi-axes, the more is Tresca peak increment. Hence the ellipsoidal shape is more dangerous than the spherical one. Whilst, In (51), the microinclusions are assumed to be spherical, and if their dimension is larger than $11 \mu\text{m}$, then an asymptotic behavior is described. For smaller inclusions, the fatigue limit is strongly reduced, and the dependence is only empirically described. Table 5 shows the Tresca peak increments corresponding to the changes in the ratio between the two semi-axes x and y (50). Respective simulations (Matrix elastic modulus E_m of 210 GPa, Inclusion elastic modulus E_h of 375 GPa, and Depth of $200\mu\text{m}$) are presented in Fig 15, Fig 16, and Fig 17.

Table 4 Effect of Shape on the stress increment

Tresca stress peak increment at NMI boundary	
Shape [y/x]	Tresca peak Increment
1	+39%
2	+42%
10	+49%

**Fig 15** % Stress increment for ratio $y/x = 1$

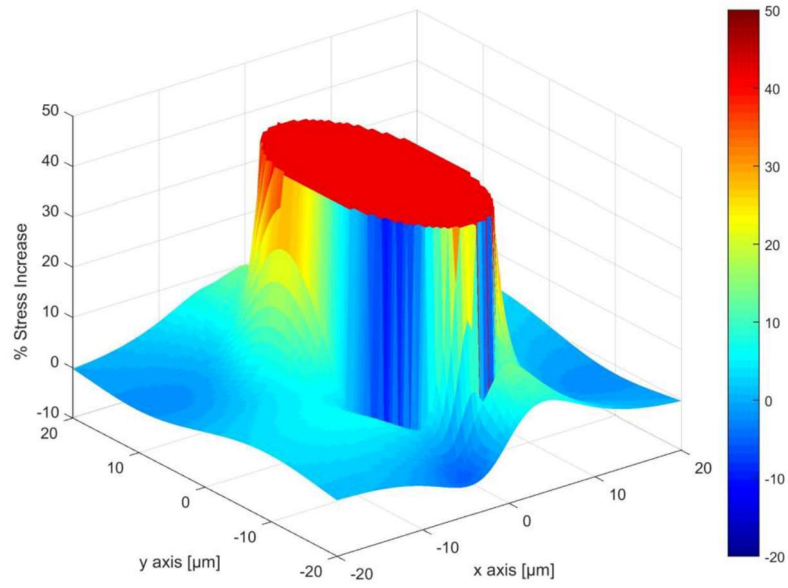


Fig 16 % Stress increment for ratio $y/x = 2$

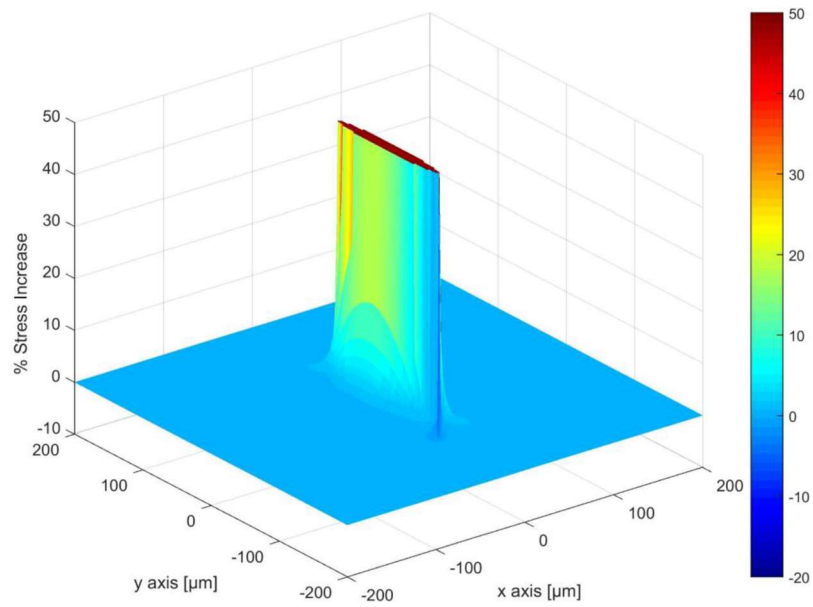


Fig 17 % Stress increment for ratio $y/x = 10$

4.2.4 Chemical composition

Non-Metallic Inclusions are stiffer than the material matrix. They are one of the most common inclusions found in the bearing steels. Alumina (Al_2O_3), Titanium nitrides (TiN), and Titanium carbides (TiC) are some of the common inclusions found in the specimens of our experimental test. An elastic modulus approximately equal to 1.8 times or higher than the elastic modulus of the pure steel makes them very detrimental. The young's modulus is similar in all of these inclusions, hence the stress peak increments remain almost the same.

Major changes in the elastic modulus (difference in E_m and E_h i.e Δ_E) will lead to larger stress peak increments. E_m and E_h are the young moduli of the matrix and the inclusion respectively. Murakami et al. (4) observed the same, i.e high elastic modulus inclusions cause higher stress peaks. And a critical value of defect depth (0.75 times the contact half-width b) can be defined, where the Von Mises stress is maximum. In the same study, a larger range of inclusion (dimensions: 5-20 μm) was investigated, observing variation in stress areas, not the maximum stress values. The other type of inclusions found in steel can be neglected as they are less stiff.

Simulation conditions (50):

- Elastic modulus of the matrix: 210 GPa
- Elastic modulus of the inclusion TiN: 380 GPa
- Elastic modulus of the inclusion TiC: 375 GPa
- Elastic modulus of the inclusion Al_2O_3 : 375 GPa
- Depth: 200 μm
- Aspect ratio (y/x) = 10

Table 6 (50) shows the stress peak increments being approximately the same, for different NMIs found in our setup. Another crucial parameter, the Poisson ratio (ν_m and ν_h), the index of the shrinkage, and the expansion of

the sample is similar to the Young modulus i.e if the difference between ν_m and ν_h (Δ_ν) increases, so does the stress peak.

Table 5 Effect of chemical composition on stress peaks

Tresca stress evaluated for different compositions	
Chemical Composition	Tresca stress peak increment
Al ₂ O ₃	+36%
TiC	+36%
TiN	+37%

Similar to the inclusion's chemical composition, the chemical composition of the Matrix (in our case 100Cr6) influences the stress field as Young's modulus (Δ_E) and Poisson's ratio (Δ_ν) change with respect to the type of matrix. Other than the bearing steel alloy used in our case, the other alloys lead to negligible variations since the input values used in the calculation are Young's modulus and Poisson's ratio. In (1), the effect of the different compositions of microinclusion referring to processing techniques and performances are investigated, aiming at relating steelmaking, inclusion microstructure, and life.

4.2.5 Configuration

Experimental evidence shows that Inclusions appear in pairs, clusters, and stringers. The ASTM E45 Standard (53) provides a solution for the stringer case with a minimum of three particles. In this case, the stringer can be considered as a standalone inclusion with an elongated semi-axis that covers the distance between the first and last inclusion. The ASTM E45 Standard

suggests placing the particles within a certain distance limit from the centerline of the stringer. The distance between the particles should be less than a certain threshold (similar results as in table 5).

In conclusion, the stress peak at the inclusion boundary is affected by the depth at which the inclusion is located. Acknowledging the proposition that the inclusion from the surface will not be the main reason for spalling. In the present research, the stress increase was +50% for the worst case. The depth threshold (depth at which the stress is below the maximum stress) calculated by the Hertz is approximately 188% (Fig 18) of the contact width b (50). This result agrees with (6) and (4).

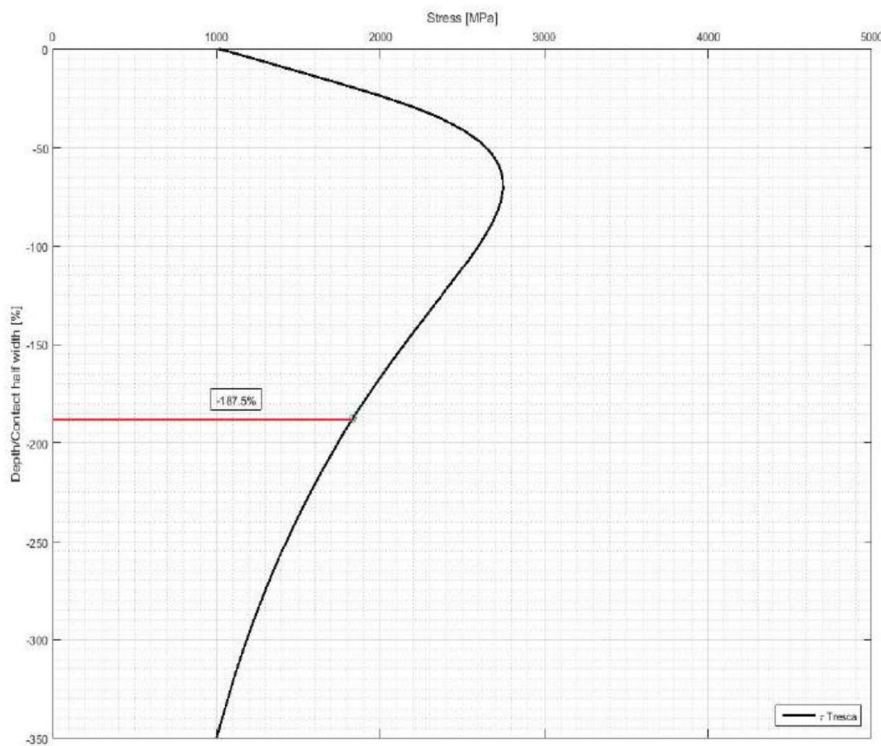


Fig 18 Depth Threshold

Chapter 5

Experimental Tests

Experimental investigations were carried out to detect the micro-inclusions and characterize them by their composition, shape, aspect ratio, geometry, and location. Unfortunately, during any manufacturing process, the material deforms, and the micro-inclusions distort. It becomes an absolute necessity to run the tests both on the raw material (standard specimen) and the processed product (bearing ball) for optimum results. Ergo, it was decided to run the experimental investigations on the raw material, assuming the results won't differ from processed steel. In regards to micro-inclusion analysis, experimental data was collected from raw material.

RCF test campaigns using a dedicated test rig were performed on the ball bearing to evaluate the fatigue life of the bearing rolling element under the influence of the micro-inclusion effect and Precessional Slip. SKF BAHB-311396B ball bearing with the ball diameter of 11.112 mm was selected. The bearing was modified to single out the failure on the bearing rolling elements (balls).

The test ends once the bearing ball fails. The failed bearing rolling elements (balls) are then subject to Fracture Analysis inspection to evaluate the origin of the fracture and subsequent parameters to make sure the failure of the ball is coming from the micro-inclusion. Based on this failure data collected, the fatigue life of the bearings was estimated and compared with the predicted results of our model.

All the experimental activities were carried out at the Pinerolo plant of Tsubaki Nakashima Co., Ltd.

5.1 Rotating Bending Fatigue Test

The Four-Point rotating bending fatigue testing machine uses a motor to rotate a specimen with a load at its center. This generates alternating stresses leading to fatigue failure of the material. Fig 19 represents the machine used in this work

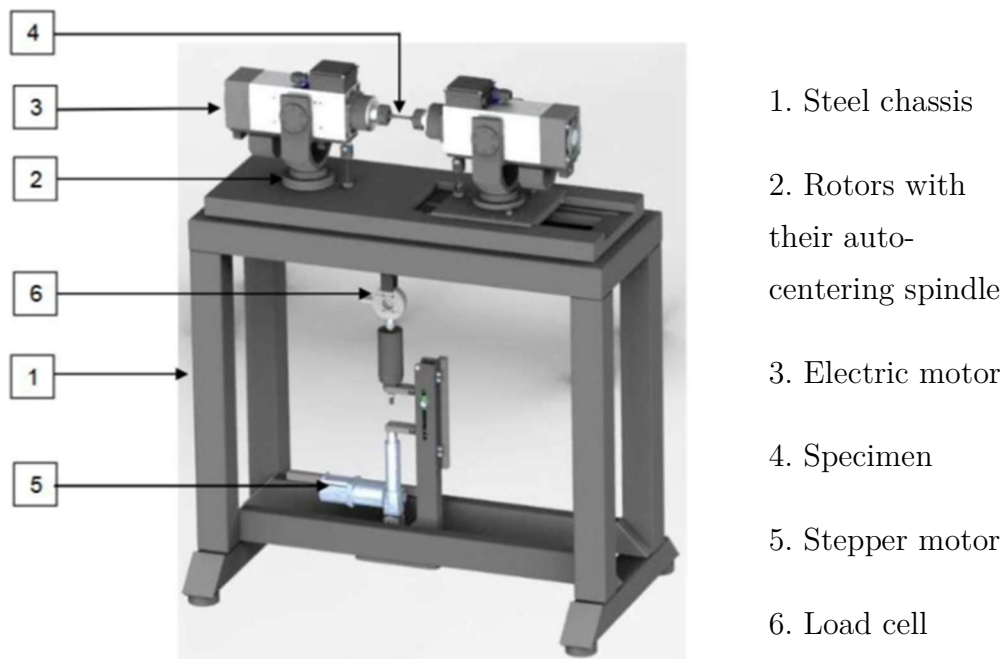


Fig 19 Rotating bending machine

In operation, the raw material is subject to rotating bending fatigue testing to detect the micro-inclusions from which the fracture was initiated. Ruptures other than inclusion-based failures are discarded. To start with, the raw material (100cr6 steel wire) is cut into 150mm samples (Fig 20).



Fig 20 Raw material and final standard specimen

The samples are then straightened to nullify the curvature of the coil. In order to duplicate the properties of the bearing's ball, the samples are quenched (for 12 minutes at 850 °C) in saltwater. Saltwater may be replaced with oil. Obeying to the standards, ISO 1143 specifications, the samples are designed into standard specimens as per the dimension of the drawing (Fig 21).

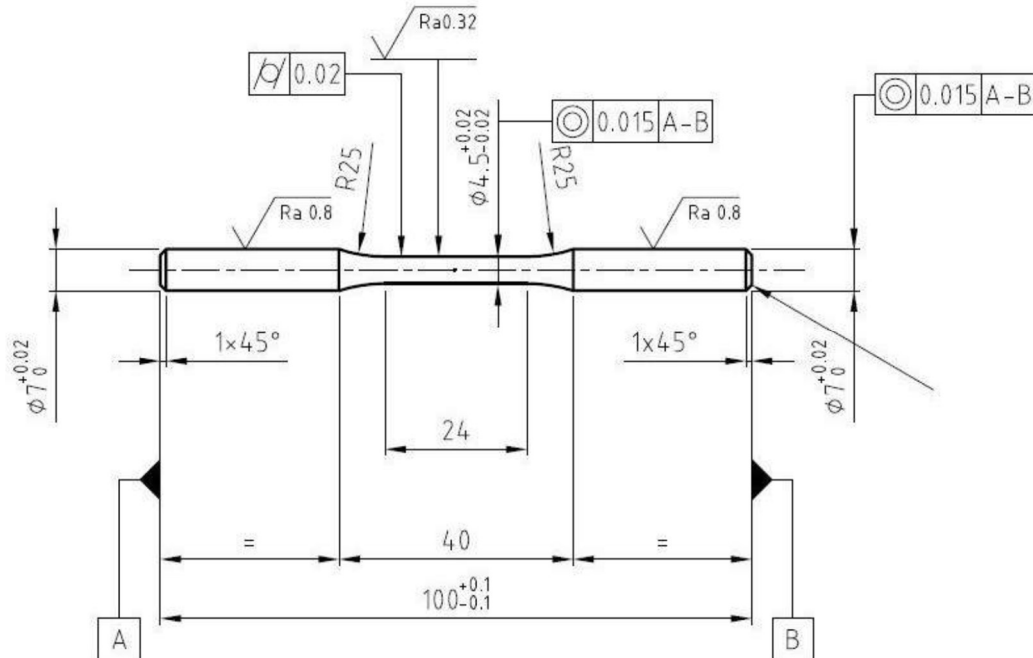


Fig 21 Standard specimen geometry

The standard specimen is modeled with a special design that creates a point of maximum stress at its midpoint rather than at its end. This gives a definite point of failure and avoids unwanted stress concentrations.

Furthermore, additional checks were made to make sure the failure of the specimen was only due to the micro-inclusion effect. The specimen was inspected with a roughness meter to avoid tangs, junctions, and central cross-sections. If any irregularities, the specimen was polished and rechecked. Visual inspection of the surface for any scratch or surface defects confirms test efficiency. To avoid rubbing the specimen within the machine, the specimen is rigidly clamped with the help of a torque wrench while the tangs were covered with a thin layer of anti-fretting paste. Low rotational speed was maintained to verify proper mounting.

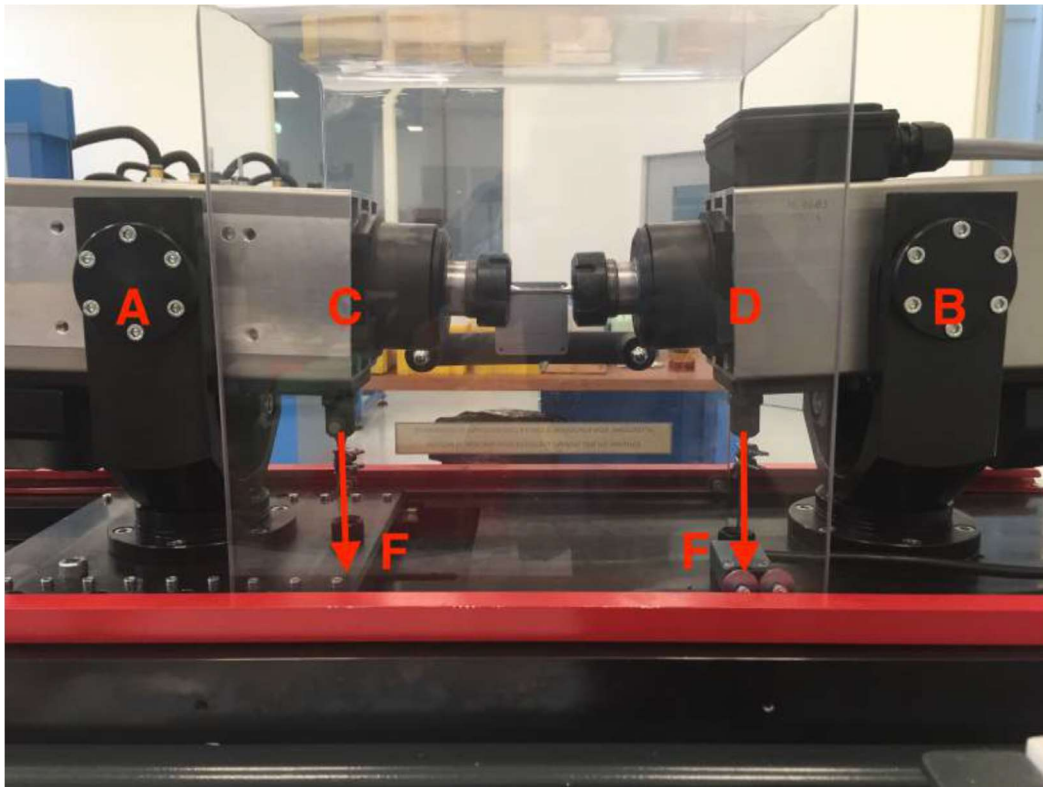


Fig 22 Four-Point Rotating Bending Test: Loading Condition

Staircase fatigue campaign was run at 3500 rpm i.e stress frequency of 58.3 Hz, life target of 5×10^6 cycles and stress increment of $\Delta\sigma$ of 25 MPa. The load applied at the minimum cross-section and the rotational speed is controlled via PC software. Fig 22 shows the loading condition.

5.2 Test rig for fatigue testing of balls

One of the prominent factors that affect the failure of the bearings is the failure of the bearing rolling element (ball). Zaretski (24) noted that bearing balls are responsible for 44.4 percent of the failures of the bearing. Whilst the inner race constitutes 44.4 percent, and the outer race to only 11.2 percent. To determine the effect of the micro-inclusions and precessional slip on the fatigue life of the bearing, mainly the bearing rolling element (ball), fatigue tests were performed using a dedicated test rig. The whole experimental setup of the fatigue tests on the bearing component was modeled in such a way that the failure of the bearing rolling element (balls) is singled out without damaging other parts of the bearing such as the inner ring, outer ring, and the cage.

Well-established process protocols were adopted to ensure the reliability of the tests carried out on multiple bearings. Same test conditions were maintained across different test runs for efficient comparison of the fatigue life of the bearings balls, affected by the presence of the micro-inclusion and the precessional motion. Failures due to excessive contact stresses, high temperatures, and vibrations were avoided.

Rigs structure

The test bench (Fig.23) consists of a shaft assembled by two 1st generation HUB bearings. One is Angular contact ball bearing (ball dia of 11.112 mm) and the other Angular contact ball bearing (ball dia of 10.50 mm).



Fig 23 Test rig benches for ball bearing test

An electric motor rotates the shaft mounting both the bearings. The bearing assembly is loaded with an axial load coming from a hydraulic piston driven by a pneumatic arrangement. The loaded section of the shaft is supported by a bearing with a ball diameter of 11.112 mm as the study is focused on this bearing. The other bearing with a ball dia of 10.5 mm functions as a support to the mounted test assembly.

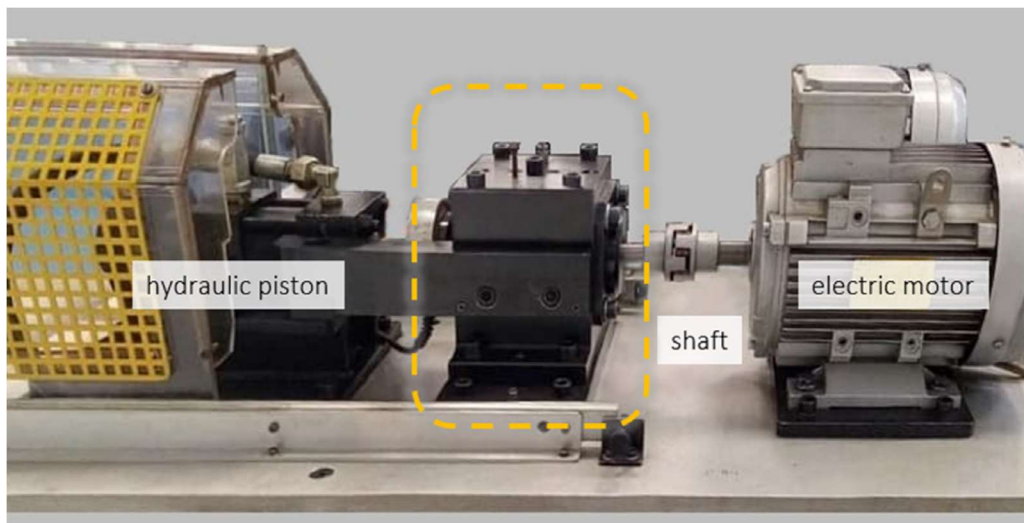


Fig 24 Test Rig close-up

The bearing is mounted on the shaft by interference fit and fixed to the structure by flanges. A protective shell covers the shaft and the hydraulic piston, allowing the operator to work safely on the other test rigs. To prevent overheating of the bearing in operation, a vent is situated above the test bearing.

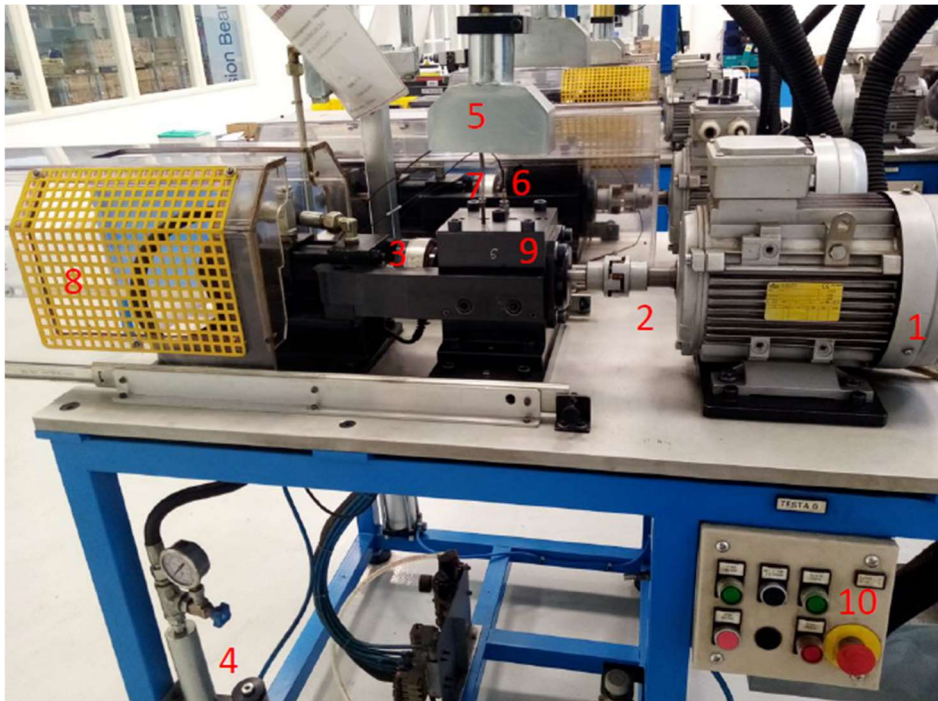


Fig 25 Test rig bench with every component labeled

Fig 25 labels all the components of the test rig assembly. The electric motor (1), shaft (2), hydraulic piston (3), pneumatic piston (4), vent (5), accelerometer (6), thermocouple (7), protective shell (8), flange (9), command system (10). A computer with dedicated software controls all these test rigs is shown in Fig 24.



Fig 26 Test rig control computer

The test bench can detect:

- Vibrations through an accelerometer
- The temperature through to a thermocouple
- Load level through to a load cell

Both the accelerometer and the thermocouple are placed on the bearing being tested (i.e bearing with balls dia of 11.112mm). Those sensors are very critical for test management as any variation from the nominal condition may be vital. Vibrations, temperature, and load level of the ongoing test rig campaign are displayed in real-time on the computer monitor. Data on temperature and vibrations are recorded once every minute for failure analysis.

A high level of load may produce high pressure on balls that leads to premature failure. A high temperature can arise due to excessive or limited

lubricant, or a marked roundness of the balls and so excessive contact pressure. A high level of vibrations may suggest a marked roundness of the balls or a failure of one of the bearing components.

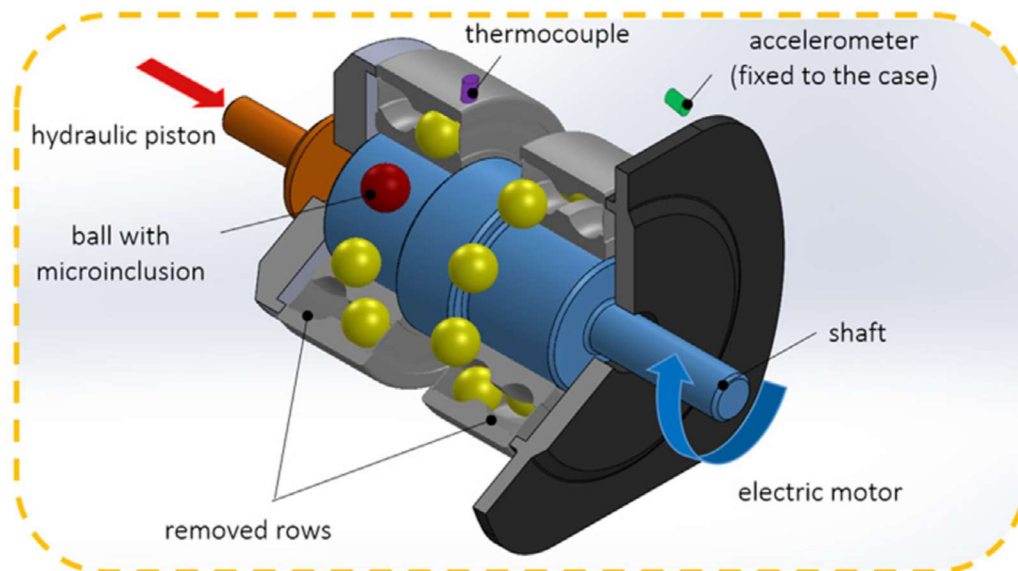


Fig 27 Test Bearing modification

As mentioned before, the whole experiment is set up in such a way that the failure on the ball is singled-out. This can be done by increasing the contact pressure between the bearing rolling elements (test balls) and the rings. Hence, only 7 balls were loaded (instead of 14 balls) in a single row of a double row test bearing(Fig 27). Loading one only row is necessary since the load applied is unidirectional. In the non-test bearing as well, only one cage is assembled as explained for the test case, but with a complete set of 15 balls.

Test procedure

The test conditions are summarized below:

- Ball diameter: $\phi 11.112\text{mm}$
- Ball material: 100Cr6
- Ball number in each test bearing: 7
- Ball number in each no-test bearing: 15
- Applied Load: 34400N
- Grease for tested balls: Shell Gadus S3 V220
- Grease for no tested balls: Shell Gadus S2 V100
- Load limit: 37500N
- Vibration limit: 15 mm/s²
- Temperature limit: 145 °C
- Shaft speed: 690 Rpm
- Life target: 200h

The test is started immediately after assembling the bench by mounting both the bearings on the shaft. For the first 10 minutes of the test run, only 30% of the nominal load is applied, to obtain a homogeneous distribution of the lubricant, and the optimal centering of the shaft. After 10 minutes of run time, the load is raised to its nominal value. Every 5 minutes the load was released for 25 seconds to facilitate the spinning of the balls. Every 20 hours the rigs are stopped, and the rings, lubricant, cages, and the balls of the non-test bearing are changed. The roundness and weight of the balls is measured to know the damage evolution. At every stop, the bench is disassembled and cleaned. The components are thoroughly inspected. This helps in preventing failures of components of the test bearing other than bearing test balls.

Test rigs are prematurely interrupted if any of the following mishaps occur:

1. **High temperature** : The test run was interrupted whenever the setup temperature crossed the tempering temperature of the test material. Above tempering temperature, the material (specifically bearing rolling element) undergoes microstructural changes (hardness reduction) which leads to reduction of fatigue life. Steels tempering temperature is 150°C. As a safety, the machine was interrupted for a temperature above 145°C.
2. **Load**: To prevent overloading, the test is stopped if the load limit is exceeded.
3. **Vibrations**: When the vibrations level is higher than 15mm/s², the machine is stopped. This threshold was chosen based on the testing experience. Compared to the nominal limit, if a lower level is set, the machine would stop for external vibrations. And if a higher level is chosen, the ball could break while the machine may continue to run.

The test ends for following three cases:

- Failure of the test balls.
- Excessive vibrations or temperature, due to a marked roundness of the balls, the test is considered failed.
- Life target is reached, the test is considered survived.

5.4 Fracture Analysis

Both the failed specimens coming from Four points rotating bending test and failed balls from Test Rig are subjected to inspection under Fracture Analysis. The origin of fracture is analyzed to ensure that the failure started from inclusion. The dimensions, shape, chemical composition, and depth of the micro-inclusion are determined.

5.4.1 Failed ball - Test Rig



Fig 28 Stereomicroscope

. Test Rig campaign finishes when the bearing fails (ball). A preliminary stereomicroscope (Fig 27) inspection is carried out on each failed ball for a better understanding of the origin of the fracture, and to evaluate whether the fracture started from the micro-inclusion. The fractured area is photographed at different levels of magnification. Analysis of these magnified images helps in identifying whether or not the inclusion caused the failure.



Fig 29 Gauge Meter

The depth of the micro-inclusion is measured using a Gauge meter.

Scanning Electron Microscope (SEM) analysis



Fig 30 Scanning Electron Microscope (SEM)

If the micro-inclusion is found in the fractured area, a Scanning Electron Microscope (SEM) analysis is carried out. A Scanning Electron Microscope (SEM) is a type of electron microscope. It uses a focused beam of electrons to scan the surface of the sample and generates magnified images for evaluation. The electrons interact with atoms in the sample producing various signals that contain information about the surface topography and

composition of the sample. Different elements produce different signals, therefore the chemical composition of inclusion is identified.

Failed Specimen - Rotating bending test

Similar to failure analysis of the failed ball, A preliminary stereomicroscope inspection is carried out on each failed specimen for a better understanding of the origin of the fracture, and to evaluate whether the fracture started from the micro-inclusion. The distance of the micro-inclusion from the surface was measured using a gauge meter. The dimension and chemical composition of the micro-inclusion was evaluated by SEM analysis.

Chapter 6

Micro-Inclusion Model.

The Fracture Analysis data concerning the dimension, composition, and depth of the microinclusion is obtained from the experimental investigation. The test campaigns were run on the standard specimen and the bearing rolling element. The resultant fracture analysis data is fed into the micro-inclusion model. This model helps in relating the life of the bearing rolling element with micro-inclusion parameters.

The Eshelby model allows the computation of the stress field inside an ellipsoidal inclusion. Mura (54) integrated this Eshelby model to the Eshelby-Mura model (54) which allows the computation of the stress distribution at the microinclusion boundary given location, dimension, aspect ratio, and composition of the microinclusion. Moschovidis (55) integrated the model by considering the effect of the interaction between microinclusions when they are close to each other.

6.1 Eshelby-Mura Model

Based on the experimental data on ellipsoidal micro-inclusion parameters, the Eshelby model allows computing the stress field surrounding it. The inclusion undergoes shape and size change when present in infinite homogeneous, isotropic, and elastic medium (matrix). Under the constraint of the matrix, the inclusion has an arbitrary homogeneous strain. The objective is to evaluate the elastic fields of the inclusion and the matrix (45).

Eshelby investigated the elastic fields by removing the matrix surrounding a generic region (inclusion). Doing this unconstrains the inclusion and facilitates its shape change. By applying force to the region, the shape of the inclusion is restored to its original. The inclusion is then put back into the matrix. As a result, the stress inside the inclusion will be constant (null). The applied surface tractions become a built-in layer of body force spread over the interface between matrix and inclusion. To complete the solution, the unwanted layer is removed by applying an equal and opposite layer of body force. The additional elastic field introduced is found by integration, from the expression for the elastic field of a point force (45).

Eshelby found the inclusion stress is uniform for ellipsoidal inclusion embedded in matrix subject to homogenous load. Meaning, the elastic stress, and strain won't change inside the inclusion.

Mura (54) defined inclusion as a subdomain Ω within a domain D . The Eigen strain $\epsilon_{ij}^*(x)$ is given in Ω and zero in $D - \Omega$. As the elastic modulus is the same for both subdomain and domain, this poses an inclusion problem. The displacement u_i , strain ϵ_{ij}^* , and stress σ_{ij} are estimated by the following expressions given in (54)

$$u_i(x) = -C_{klmn} \int_{\Omega} \epsilon^*(x') G_{ij,k}(x-x') dx' \quad (6.1)$$

$$\epsilon_{ij}(x) = -\frac{1}{2} \int_{\Omega} C_{klmn} \epsilon_{mn}^*(x') (G_{ij,k}(x-x') + G_{ij,k}(x-x')) dx' \quad (6.2)$$

$$\sigma(x) = -C_{ijkl} \int_{\Omega} C_{pqmn} \epsilon_{mn}^*(x') G_{kp,ql}(x-x') dx' + \epsilon_{kl}^*(x) \quad (6.3)$$

where C_{ijkl} is the stiffness tensor, G_{ij} is Green's function, x is the position vector. x' denotes the position of a point source. A point source is a single identifiable localized source. It has a negligible extent, distinguishing it from other source geometries. Point sources in mathematical modeling are usually approximated as mathematical points to simplify analysis.

But since the stress and strain fields inside the inclusion are uniform, the strain field inside the inclusion becomes

$$\epsilon_{ij}(x) = S_{ijkl} \epsilon_{kl}^* \text{ for } x \in \Omega \quad (6.4)$$

where S_{kl} is the Eshelby tensor (4). This tensor contains several integrals, approximated with a tolerance of the order 10^{16} by the MATLAB function `elliptic12` (56). The solutions are quasi-analytical (4).

While the strain field outside the inclusion is given by

$$\epsilon_{ij}(x) = S_{ijkl} \epsilon_{kl}^* \text{ for } x \in D - \Omega \quad (6.5)$$

Now that, the strain field both inside and outside the inclusion is determined, the stress field can be approximated as

$$\sigma_{ij}(x) = C_{ijkl} \epsilon_{kl}(x) \quad (6.6)$$

6.1.1 Equivalent Inclusion Method

As we have already discussed, Mura (54) integrated the Eshelby model. Eshelby - Mura model (54) allows calculating the stress distribution at the microinclusion boundary: given the location, dimension, aspect ratio, and composition of the microinclusion.

When the elastic field is characterized by different elastic moduli i.e the subdomain moduli is different from the matrix moduli. This is an “inhomogeneity problem”. If the same elastic moduli, then it's an “inclusion problem”. A correlation between the two was argued by Eshelby (45) i.e the stress perturbation due to the presence of an ellipsoidal inhomogeneity of a homogeneous applied stress (σ_{ij}^∞) can be determined by an inclusion problem when the Eigen strain ϵ^* is chosen correctly. This is called the Equivalent Inclusion Method (57).

Now, the strain and stress fields around the inclusion are given by (54)

$$\epsilon_{ij} = \epsilon_{ij}^\infty + S_{ijmn} \epsilon_{mn}^* \quad (6.7)$$

$$\sigma_{ij} = \sigma_{ij}^\infty + C_{ijkl} (S_{klmn} \epsilon_{mn}^* - \epsilon_{mn}^*) \text{ for } x \in \Omega \quad (6.8)$$

$$\epsilon_{ij}(x) = \epsilon_{ij}^\infty + D_{klmn}(x) \epsilon_{mn}^* \quad (6.9)$$

$$\sigma_{ij}(x) = \sigma_{ij}^\infty + C_{ijkl} (D_{klmn}(x)) \epsilon_{mn}^* \text{ for } x \in D - \Omega \quad (6.10)$$

Note: Equations (6.7) and (6.9) are similar to (6.4) and (6.5) respectively. But, the equations describing the equivalent inclusion method (6.7) and (6.9) have the term ϵ_{ij}^∞ which represents a remote strain induced by the homogeneous stress σ_{ij}^∞ . The same goes for the equations concerning the stress (6.8) and (6.10). But, in these equations the Eigen strain is stress-free.

It has to be subtracted from the total strain while calculating the stress inhomogeneity.

6.2 Matlab Solver

A 3D numerical MATLAB solver based on the Eshelby solution was used to evaluate the effects of various types of inclusions and matrices. Mainly to determine the stress field around the microinclusion. Healy (58) proposed a MATLAB code that was able to consider the Eshelby solution for inclusion with semiaxes $a_1 = a_2 \neq a_3$. But, the Matlab code used in this thesis is based on Meng et al (57). This code solves for the general ellipsoidal inclusion or inhomogeneity with three different semiaxes. This code was further modified to adapt to our specific case of inclusions in ball bearings. As explained by Meng et al. (57), the main script, **incl_prob.m** handles the input data structure, calls the Eshelby solver, **Esh_sol.m**, and presents the results.

The input structure **incl** has the following attributions:

- E_m : Young's modulus of the matrix
- ν_m : Poisson ratio of the matrix
- E_h : Young modulus of the inhomogeneity
- ν_h : Poisson ratio of the inhomogeneity
- *dim*: the ellipsoidal dimensions a_i
- *ang*: rotation angles around coordinate axes
- *stressvec*: remote stress σ_{ij}^∞
- *eigp*: initial eigenstrain ϵ_{ij}^p
- *grid*: observation grid(s) evaluate the solutions

where the stress and strain tensors are in the form of six-component vectors because of the symmetry. The **Esh_sol.m** function reads the input

data and outputs the arguments, “disp”, “stress”, and “strain”. The routines called by this function are in the order of appearance.

Ctensord.m constructs the stiffness tensors C_{ijkl} and C_{ijkl}^* for the given moduli (E_m, ν_m) and (E_h, ν_h) . From stress-strain (eqn (6.6)), it is possible to calculate the remote strain ϵ_{ij}^∞ for the remote stress σ_{ij}^∞ . Also, if $C_{ijkl} = C_{ijkl}^*$, then $\sigma_{ij}^\infty = 0$ and $\epsilon_{ij}^p \neq 0$. This is the original inclusion problem.

Esh_int.m constructs the Eshelby tensor S_{ijkl} for a given ν_m and ellipsoid dimension a_i . With C_{ijkl}^* , ϵ_{ij}^∞ and S_{ijkl} it's possible to calculate the fictitious Eigen strain (ϵ_{ij}^*). **Esh_D4.m** constructs the tensor $D_{ijkl}(x)$ for the given ν_m , a_i and coordinates x_i . With D_{ijkl} , it is possible to calculate the exterior strain and stress. **Esh_disp.m** constructs the displacements u_i for the given ν_m , a_i , x_i , and ϵ_{ij}^* . **Esh_D4_disp.m** merges the functionalities of **Esh_D4** and **Esh_disp**. Owing to our objective, which is to estimate the stress field perturbation, only the **Esh_D4** routine is chosen. The displacement given by the **Esh_disp** is not considered at this stage.

6.3 Statistics of Extreme Values Method

To identify the statistical distribution of the Non-metallic Inclusion in the material matrix, a preliminary Statistical analysis of the Extreme Values (SEV) was performed. The stress peak at the inclusion boundary does not depend on the inclusion size. However, it is important to define the critical dimension. Concerning the steel properties, Large oxide inclusions are much more dangerous and harmful than the smaller ones. A safe critical inclusion size is defined.

SEV method is used to mathematically explain the observed extremes in the samples of specified sizes. In our case, the presence of the largest inclusion in the fixed volume, along with the probability that, found inclusion is larger than a critical size. In literature, this approach is already applied in many fields related to metals. Murakami and his coworkers (59) were the first to apply this method. In their study, the size of the largest inclusion in a large volume of steel was estimated based on data acquired from a polished surface. Extreme value theory's basis is: among a fixed set of collected data points following a basic distribution, the maximum and minimum of each of these sets also follow a distribution (60)

The distribution is given by the following function (eqn 6.11) in (60):

$$G(z) = e^{-e^{-\frac{z-\lambda}{\alpha}}} \quad (6.11)$$

where $G(z)$ is the probability that the largest inclusion is no larger than size z . α and λ are the scale and location parameters.

Introducing reduced variate $y = \frac{z-\lambda}{\alpha}$ in eqn 6.11

$$H(z) = e^{-e^{-y}} \quad (6.12)$$

To determine the characteristic size of the largest inclusion in a defined volume V , a standard inspection area S_0 (mm^2) is defined. The square root of the maximum area of inclusion area gives $(\sqrt{Area_{max}})$. This is repeated for N areas. The values of $(\sqrt{Area_{max,i}})$ are ranked, starting from the smallest with $i=1,2,\dots,N$.

The cumulative probability of inclusion size z_i is calculated by

$$H(y_i) = \frac{i}{N+1} \quad (6.13)$$

From equation 6.12

$$y_i = -Ln\{-Ln[H(y_i)]\} \quad (6.14)$$

Defining h as the mean value of $(Area_{max,i})^{\frac{1}{2}}$ gives

$$h = \frac{\Sigma(\sqrt{Area_{max}})}{N} \quad (6.15)$$

The standard inspection volume V_0 is

$$V_0 = h \times S_0 \quad (6.16)$$

The return period T will be

$$T = \frac{V}{V_0} \quad (6.17)$$

From equation 6.11, the distribution $G(z) = 1 - \frac{1}{T}$ then

$$y(T) = -Ln\left(-Ln\left(\frac{T-1}{T}\right)\right) \quad (6.18)$$

$(\sqrt{Area_{max}})$ is plotted in terms of y_i , then a straight line joining the best approximates the data points is drawn. The abscissa of the intersection point between $y_i = y(T)$ and the straight line is found. The of this point is the square root of the characteristic size of the maximum inclusion. From $y = \frac{z-\lambda}{\alpha}$ and the experimental straight line, α and λ are calculated. Finally from eq. (6.11) the probability that the largest inclusion is no larger than critical size z is calculated.

6.3.1 Cleanliness Analysis

A microscopic inspection of the polished specimen (raw-material) surface section to find the inclusions. According to ASTM E45 (53), in this microscopic method of examination, inclusions are assigned to a category based on similarities in morphology, but not necessarily on their chemical identity. Inclusions are characterized by size, shape, concentration, number, type, and distribution rather than by chemical composition. Despite the compositions being not identified, microscopic methods characterize inclusions into one of several composition-related categories. The most common of them are

- Sulfides
- Aluminates
- Silicates
- Oxides

Microscopic inspection is done by examining the specimen with a light microscope and reporting the types of inclusion encountered, accompanied by a few representative photomicrographs. Standard reference charts depicting a series of typical inclusion configurations (size, type, and number) will assist in direct comparison with the generated microscopic field of view.

The minimum polished area of a specimen for the microscopic determination of inclusion content is 170 mm². Specimens with polished flat surfaces are appreciated as they generate microscopically flat section outputs. The shape and size of the inclusion can be seen more accurately.

To obtain satisfactory and consistent inclusion ratings, the specimen's polished surface must be free of artifacts such as pitting, any foreign materials, and scratches. While polishing the specimen care must be taken to avoid inclusion getting pit, dragged, or obscured. Specimens must be examined in the as-polished condition, free from the effects of any prior etching (if used). Inclusion retention is generally easier to accomplish in hardened steel specimens than in the annealed condition. If inclusion retention is inadequate in annealed specimens, they should be subject to standard heat treatment cycles using a relatively low tempering temperature. After heat treatment, the specimens are descaled, and the longitudinal plane must be reground below any decarburization.

The samples are divided into the standard inspection area. Every standard inspection area is examined to find non-metallic inclusions.

6.3.2 Experimental data

A sample of steel 100Cr6 was divided into the standard inspection area S_0 (Fig 31). After inspection of SEV analysis 36 inclusion were found. Their resultant data collected on maximum inclusion area ($Area_{max}$), the cumulative probability of inclusion size z_i ($H(y_i)$) and (y_i) is listed in the table

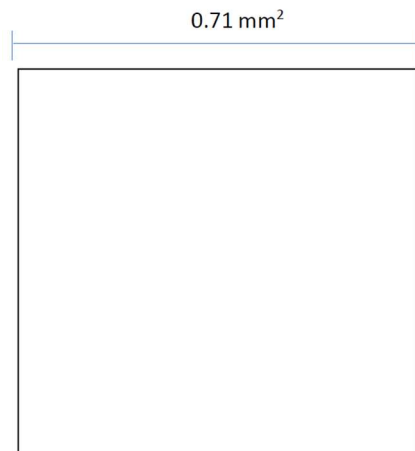


Fig 31 Standard inspection area 0.5 mm^2

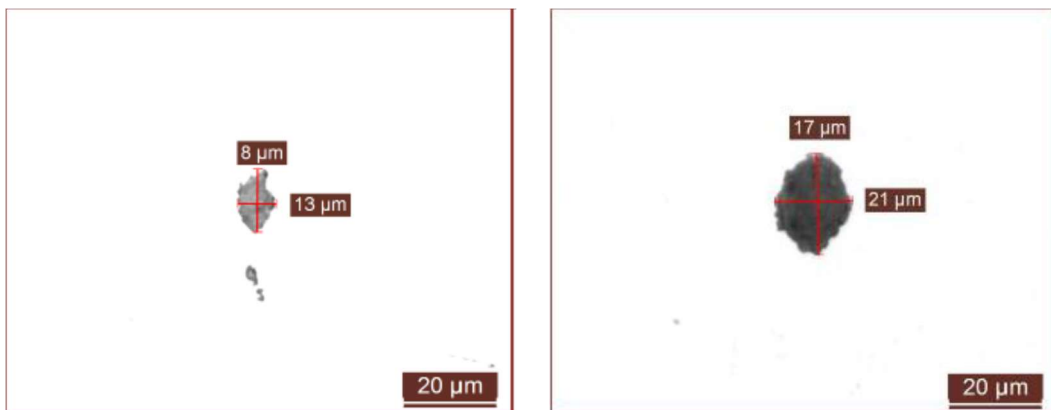


Fig 32 Examples of Inclusions found

Table 6 Data collected after Inspection

$(\sqrt{Area_{max}})$	$H(y_i)$	y_i
7,2	0,03	-1,28
7,9	0,05	-1,07
8,0	0,08	-0,92
8,4	0,11	-0,80
8,4	0,14	-0,69
8,5	0,16	-0,60
8,7	0,19	-0,51
8,8	0,22	-0,43
8,8	0,24	-0,35
8,9	0,27	-0,27
9,0	0,30	-0,19
9,3	0,32	-0,12
9,3	0,35	-0,04
9,7	0,38	0,03
9,7	0,41	0,10
9,7	0,43	0,18
11,1	0,46	0,25
11,1	0,49	0,33
11,7	0,51	0,41
12,0	0,54	0,49
12,6	0,57	0,57
12,7	0,59	0,65
12,8	0,62	0,74
13,3	0,65	0,84
13,7	0,68	0,94
13,9	0,70	1,04
14,2	0,73	1,15
14,6	0,76	1,28
15,5	0,78	1,41
15,5	0,81	1,56
16,7	0,84	1,73
16,8	0,86	1,93
19,5	0,89	2,17
21,7	0,92	2,47
23,0	0,95	2,89
23,5	0,97	3,60

Based on this experimental data, estimation of the maximum inclusion size in a large volume of steel specimen(100Cr6) by the SEV method was estimated.

Chapter 7

Integrated Life Model

To investigate the relationship between the Precessional Slip and Micro-Inclusion model with the Bearing life, an Integrated Life Estimation Model with a dedicated Numerical Solver was developed. The numerical solver was developed in MS Excel. All the resultant experimental analysis data was fed into the Integrated Solver. All the parameters concerning Precessional Slip and Micro-Inclusion effect were estimated by the solver. Further, the Bearing life i.e life of the bearing rolling element was estimated using this integrated life estimation model under the influence of transverse precessional slip and the micro-inclusion effect. These life predictions were compared with the actual experimental cycles of failure (fatigue life) to validate our Integrated Life Model.

7.1 Integrated Life Model-Relating Life with Precessional slip and Inclusion effect

Bearing life formulation using the Zaretsky model is already discussed in detail in chapter 2. This life formulation is modified to include the influence of the slip and precession motions in presence of micro-inclusion. The chapter, Ball Motions and Precessional Slip Model discusses in detail the conditions leading to slip and precession. The model also provides the formulations for the estimation of transverse slip, ball spin frequency, and micro-inclusion loading frequency.

The estimation of stress increments due to sub-superficial micro-inclusions is investigated in subsequent chapters. The Chapter on the Micro-Inclusion Model details the Equivalent Inclusion Method, Matlab solver based on Esheby code, and SEV Analysis. These methods solve for the calculation of stress distribution at the inclusion boundary, the effect of various types of inclusions, the stress field surrounding the inclusion and distribution of the inclusions in the material matrix.

Now, to relate all these parameters, a spreadsheet-based Integrated Life Solver was developed to incorporate all the above-discussed models. In this Integrated model, all the parameters accounting for precessional slip and micro-inclusion were estimated as per the sequence they are derived in their respective chapters. Once the inclusion loading frequency was determined based on the Precessional Slip Model, the corrected maximum equivalent Tresca stresses were determined corresponding to each micro-inclusion based on the results of fatigue testing and failure surface inspection.

Firstly, the nominal Hertz stress distribution was calculated. For each micro-inclusion found in failed balls and failed specimens, the maximum equivalent Tresca stress in the uniform matrix σ_{nT} and at the micro-

inclusion boundary σ_{iT} was estimated by the integrated solver based on the micro-inclusions dimension, shape, aspect ratio, position, and elastic modulus. The percent difference σ_{inc} between the two stress values was calculated as well. The maximum Tresca equivalent stresses σ_{nT} and σ_{iT} calculated at the inclusion depth was assuming the absence and the presence of the inclusion respectively. N_L is the axial load applied to the bearing during the test rig during experimental testing. H_L is the Hertz Load i.e the contact load applied to a single, homogeneous ball, generating at the microinclusion depth the same Tresca stress due to microinclusions.

The crucial parameter that helps in relating the precessional slip and micro-inclusion effect with the bearing rolling-element life is the “Equivalent dynamic Load (P_{eq})”. This parameter is present in the bearing life formulation of the Zaretsky model (eqn 2.24 from chapter 2)

$$L_{10} = LF_C \left(\frac{C_D}{P_{eq}} \right)^p \quad (2.24)$$

In our Integrated Life Estimation Model, the Zaretsky bearing life formulation was further modified. In contrast to the nominal equivalent load (P_{eqn}), A new equivalent load (P_{eqi}) which includes the influence of the precessional slip, as well as the micro-inclusion effect, was introduced. P_{eqi} is the equivalent load calculated including the averaged normal force F_{aa} acting on the ball in the presence of the defect (micro-inclusion) and the precessional slip. F_{aa} is the weighted average of the nominal load N_L applied to the bearing and the Tresca Load (T_L).

$$F_{aa} = (3N_L + T_L) \frac{1}{I_L} \quad (7.1)$$

T_L is defined as the theoretical bearing load that would produce, in a homogeneous matrix, the same equivalent Tresca stress that is given by the

microinclusion. I.e the contact force that can generate the same stress in a homogenous matrix (absence of inclusion) similar to Tresca equivalent stress generated in the presence of the inclusion. T_L is computed considering the number of balls and the contact angle. These values will be listed in the Results section. P_{eqn} is calculated as per the catalog indication i.e i.e. 0.66 times the axial force acting on the bearing. Similarly, P_{eqi} is 0.66 times the F_{aa} .

I_L is the number of shaft revolutions for which the inclusion is loaded once. This is determined from the Inclusion Loading Frequency from Precession Slip Model. Considering that the inclusion is loaded twice during a complete rotation (once with inner race and once with outer race), the I_L would be once half of $\frac{1}{R}$ shaft revolutions (from chapter 3, eqn 3.18). It is furthermore assumed that the load is effective on damaging the rolling element only if the contact occurs when the microinclusion is exactly below the contact point.

Finally, the bearing life prediction L_{10} is calculated. Nominal bearing life L_{10n} assuming the absence of the precessional slip and the micro-inclusion effect corresponding to P_{eqn} is calculated. Likewise, L_{10i} is the bearing life estimated in the presence of micro-inclusion under the influence of the precessional slip, corresponding to P_{eqi} . These predicted ball lives are compared with the experimental cycles of failure (N_f) to validate our Integrated Model. For sake of simplicity, the values of L_{10} are expressed in cycles, not in millions of cycles.

7.2 Integrated Numerical Solver

In correspondence to the integrated model discussed in the previous section, a spreadsheet-based dedicated numerical solver was developed in MS Excel. The integrated solver incorporated all the models discussed in the previous chapters. The results of Integrated Solver are reported in the next chapter.

Chapter 8

Results and Discussions

8.1 Experimental Results.

The failed specimens and failed balls coming from the rotating bending test and the test rig respectively were subject to Fracture analysis. The dimensions, shape, chemical composition, and depth of the micro-inclusion were determined by SEM analysis and Gauge meter. The results of the preliminary statistical cleanliness analysis are also reported.

8.1.1 Statistics of Extreme Values Method

Based on this experimental data collected in (table 7), estimation of the maximum inclusion size in a large volume of steel specimen(100Cr6) by the SEV method was estimated. The following parameters were calculated.

Table 7 Parameters used in SEV method

V_0 (mm^3)	V (mm^3)	h (μm)	N	T	$y(T)$
6.2	267.79	12.4	36	42.9	3.75

A volume V of an annulus with an external diameter of 11.112 mm and the depth threshold (800 μm) was chosen. The stress peak due to a potential inclusion should remain below the maximum stress of the steel matrix at the chosen volume. Experimental data used in this study of SEV analysis is collected from the raw materials. Unfortunately during any manufacturing process steel deforms and the inclusions get distorted. Hence, it was decided to run the inspection on raw materials assuming that the test result data obtained from the raw material won't differ from the data obtained from processed steel.

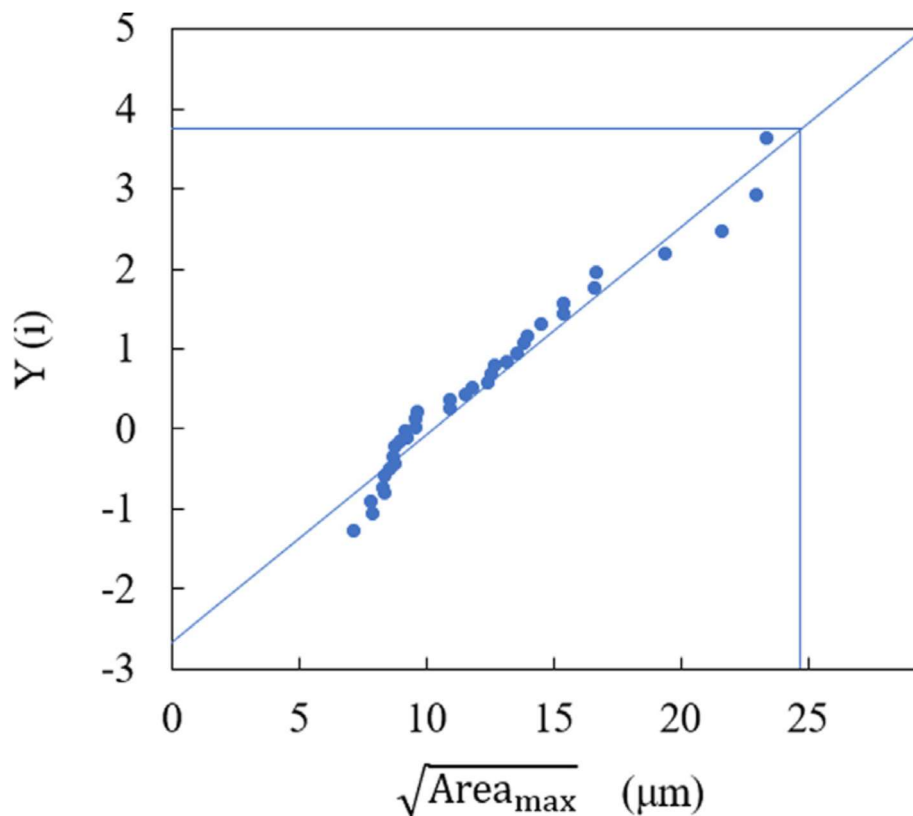


Fig 33 Estimation of the maximum inclusion size in a volume of 100Cr6 steel by the SEV method.

From Fig 23, $y(T)$ can be estimated to $y(T) = 3.75$. The slope of the line can be approximated to $\frac{1}{\alpha} = 0.2582$. The intersection between the

vertical axis and the approximated line is $\frac{\lambda}{\alpha} = -2,658$. $\sqrt{Area_{max}} = 616 \text{ mm}^2$.

In Table 9 the probability that the largest inclusion is no larger than a fixed $\sqrt{Area_{max}}$ changes are estimated. The fixed size dimensions of 5, 10, 15, 20, and 25 μm are used.

Table 8 Probability that the largest inclusion is no larger than a fixed $\sqrt{Area_{max}}$

$(\sqrt{Area_{max}}) \mu\text{m}$	5	10	15	20	25
$G(\sqrt{Area_{max}}) \mu\text{m}$	2%	34%	74%	92%	98%

8.1.2 Four-Point Rotating Bending Test on Specimen

The results of fracture analysis on the failed specimens coming from the Four-Point rotating bending fatigue tests are reported along with the dimensions, shape, chemical composition, and depth of the micro-inclusion. The last column reports the actual life of the tested specimens in the number of cycles to failure.

Table 9 Results of fatigue testing on specimens

Case	Inclusion composition	Inclusion dimension [μm]			Inclusion depth [μm]	Cycles to failure (10^6)
		x	y	z		
1	Al_2O_3	17.5	17.5	17.5	-245	2.80
2	Al_2O_3	13.5	13.5	13.5	-85	1.36
3	Al_2O_3	12.5	12.5	12.5	-80	2.74
4	S, Ca, Mn	12.5	12.5	12.5	-142	10.10
5	Al_2O_3	13.0	13.0	13.0	-34	0.77
6	Al_2O_3	12.0	12.0	12.0	-74	0.62
7	Al_2O_3	11.5	11.5	11.5	-138	0.06

Only seven failure cases had inclusion identifiable in them among the 12 test specimens run. Those seven specimens with inclusion were analyzed. Al_2O_3 was the most common one. The inclusion from which the fracture started, was composed of Al_2O_3 plus other oxides in five of the cases. Only in one case was the Aluminum was not found in the specimen. The remaining specimens had an inclusion but probably broke off when the rupture happened, so it was not possible to identify its composition.

As Al_2O_3 was the common inclusion composition found in most of the cases, Young's modulus and the Poisson's ratio of Al_2O_3 is considered for calculation for all the cases. Also, it will become complicated to account for every element found in the inclusion composition. From the table, it is evident that the dimension and the depth in each case of all the inclusion

are similar in their coordinates. Hence, the inclusion size can be approximated to circular. No more than one inclusion was present in the fractured area.

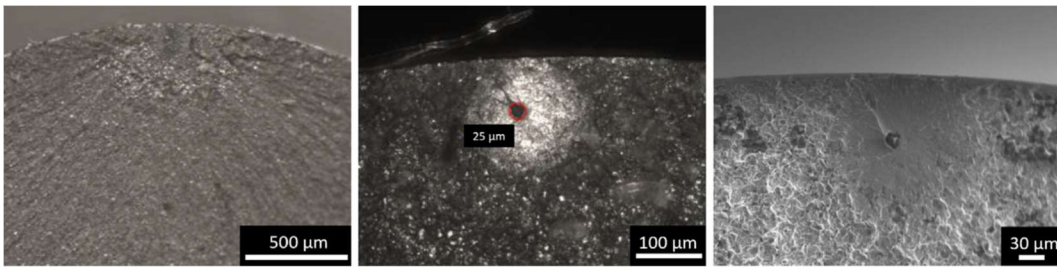


Fig 34 Case 3: Micro-inclusion crater in the specimen
(**63x, 200x, 800x**)

Considering case 3 from the table, the microinclusion was not easily identifiable in the fracture area. However, it was possible to recognize the crater where the inclusion was located (Fig. 34). The figure shows the failed specimen at different levels of magnification. The dimension of the crater was assumed as microinclusion dimensions and the traces of the element found in the craters helped in defining the microinclusion composition.

8.1.3 Fatigue Tests on Bearing Balls

The results of fracture analysis on the failed balls coming from the Test rig campaigns are reported along with the dimensions, shape, chemical composition, and depth of the micro-inclusion. The last column reports the actual life of the tested bearing balls in the number of cycles to failure.

Table 10 Test rig - Ball fatigue and failure inspection results

ID	Composition	Dimension [μm]			Depth [μm]	Aspect Ratio	N_f
		x	y	z		xy-plane	10^6 Cycles
1	TiC	1.7	4.3	1.7	-453	0.4	0.46
2	Al_2O_3	1.7	2.7	1.7	-562	0.63	1.4
3	Al_2O_3	7	49	7	-600	0.14	1.94
4	Al_2O_3	12.5	12.5	12.5	-284	1	0.87
5	TiC	4.5	4.5	4.5	-436	1	1.45
6	Al_2O_3	12.3	10	10	-326	0.81	0.46
7	Al_2O_3	3.5	2	2	-450	0.57	3.75
8	Al_2O_3	2.5	0.5	0.5	-636	0.2	1.28
9	Al_2O_3	4	1	1	-386	0.25	0.61
10	Ca Oxide	4	2	2	-580	0.5	0.97
11	Al_2O_3	7.5	7.7	7.5	-535	1	0.54
12	Si+Al+Ca	15	15	5	-327	1	0.87

Twelve broken balls coming from the test rig were analyzed. More than one inclusion was found in five cases of the 12 cases. Of the inclusion found, the inclusion corresponding to a major increase of stress was considered. The reason is, the inclusion with the largest stress increment is vital from a

fatigue life point of view. Additionally, if inclusions with different chemical compositions were detected, a weighted average of Young's modulus and Poisson's ratio of the found inclusions was considered for evaluation.

8.2 Integrated Numerical Solver

8.2.1 Ball Local Reference Frame

Based on the typical geometrical parameters of the Ball Bearing SKF BAHB-311396B (Ball material: 100Cr6) used in our experimental analysis, the results of vectors defining the ball local reference frame are tabulated. The calculations use an Eulerian reference system to describe precession and are for the counter-race rotation mode with zero ball orbit rate.

Table 11 Ball Reference System

BALL LOCAL REFERENCE SYSTEM			UNITS
Bearing Outer Diameter	D_o	72.00	mm
Bearing Inner Diameter	D_i	39.00	mm
Bearing Pitch Diameter	E	56.50	mm
Ball Diameter	d	11.112	mm
Number of Balls	N	7.00	units
Contact Angle	B or φ	20.00	°
enter \mathbf{i}'	i'	1.00	mm
enter \mathbf{j}'	j'	1.00	mm
enter \mathbf{k}'	k'	1.00	mm
enter Ball Index (n=1,2,3..,7)	n	1.00	units
Ball spacing angle	a	22.68	°
Vector \mathbf{i}_n (normal to hertz contact area)	i_n	-0.60	-
Vector \mathbf{j}_n (in the rolling direction)	j_n	1.00	-
Vector \mathbf{k}_n (across rolling direction)	k_n	1.28	-

The local reference frame vectors results are close to 1. This validates the condition from the literature (29) that, for any typical angular contact ball bearing these vectors must be close to unity.

8.2.2 Ball Angular Velocity with Precession

The result of the angular velocity (δ'_n) of the ball precessing in counter-rotation is solved by the integrated numerical solver (table 13). The two oblique components of the precessing velocity, spin vector s along the ball hole axis and the precession vector p of the ball hole axis were calculated by solving for the expression from Eqn. (3.2) and Eqn. (3.3) from chapter 3 with respect to our experimental condition. The precession angle θ was obtained from the experimental setup. It depends strongly on lubrication conditions.

Table 12 Ball Precessional Velocity

BALL ANGULAR VELOCITY WITH PRECESSION			UNITS
enter Spin Vector	s	- 0.46	N.mm.min
enter Precession Vector	p	8.80	mm.min
enter Precession Angle	θ	30.00	°
enter time	t	1.00	min
Ball Angular Velocity Vector	δ'_n	9.10	rad/min

p and θ may be obtained separately through the stroboscope experimentally. But, due to lack of detailed measurements, θ was assumed in the present integrated model.

The spin vector's result, $s = -0.46$ is negative. This means the spin and the precession motions point more or less in opposite directions. Thus, the precession motion is retrograde in our case. Since the ball's precessing angular velocity is the function of time, for the sake of simplicity, time was assumed as 1 min.

8.2.3 Surface Velocities at Ball-Race contact

The radius vectors and the surface velocities of the ball and race at both inner and outer contacts are calculated.

Table 13 Ball and Races surface velocities

BALL-RACE CONTACT VELOCITY			UNITS
enter $\dot{\gamma}'_i$	$\dot{\gamma}'_i$	1.00	-
enter $\dot{\gamma}'_j$	$\dot{\gamma}'_j$	1.00	-
enter $\dot{\gamma}'_k$	$\dot{\gamma}'_k$	1.00	-
Radius Vector to Ball Outer contact	$r_{B(o)}$	-3.32	mm
Radius Vector to Ball Inner contact	$r_{B(i)}$	3.32	mm
Ball Surface Velocity Vector at Outer contact	$V_{B(o)}$	55.52	mm/min
Ball Surface Velocity Vector at Inner contact	$V_{B(i)}$	-55.52	mm/min
Outer Race Angular Velocity Vector	$\dot{\gamma}'_o$	1.73	rad/min
Inner Race Angular Velocity Vector	$\dot{\gamma}'_i$	-1.73	rad/min
Radius Vector to Ball Outer Race contact	r_o	4.13	mm
Radius Vector to Ball Inner Race contact	r_i	2.84	mm
Outer Race Surface Velocity Vector	V_o	7.15	mm/min
Inner Race Surface Velocity Vector	V_i	-4.92	mm/min

where γ_{ijk} is the magnitude of race angular velocity vector $\boldsymbol{\gamma}_{o(i)}$ at outer and inner contact. The outer surface velocity vector V_o is critical in calculating the inclusion loading frequency.

8.2.4 Precessional Slip and Pure Spin at Ball-Race Contact

The results of the slip velocities at ball-race contact with precession and spin velocities in ordinary conditions are calculated. The differences between Slip Velocities with and without Precession (pure spin) at Ball-Race contact are compared.

Table 14 Slip and Spin velocities at Ball-Race contact

BALL-RACE SLIPS		UNITS	
Outer Ball -Race Slip Velocity Vector	$V_{s(o)}$	-7.68	mm/min
Inner Ball-Race Slip Velocity Vector	$V_{s(i)}$	91.81	mm/min
For Pure Spin, $\mathbf{p}=\boldsymbol{\theta}=\mathbf{0}$, and $\boldsymbol{\delta}=\mathbf{s}$, which gives			
Outer Ball-Race Slip Velocity Vector	$2V_{s(o)}$	-14.85	mm/min
Inner Ball-Race Slip Velocity Vector	$2V_{s(i)}$	180.87	mm/min

The above results (Table 15) on precessional slip and pure spin velocities demonstrate that the slip velocities with precession motion are about one-half to that of pure spin.

8.2.5 Basic Speed Ratio with Precession

The results of the total bearing speed and generalized basic speed ratio with precession are reported.

Table 15 Bearing speed and speed ratio

PRECESSIONAL SPEED RATIO			UNITS
Total Speed of Bearing	S	3.46	rev/min
BASIC SPEED RATIO with Precession	ρ_p	2.46	rev/min

The basic speed ratio is calculated through the integrated solver by approximating the generalized expression (eqn 3.13) from chapter 3. To confirm this result of the basic speed ratio with precession solved by the Integrated solver, we can opt for the basic speed ratio definition. By definition, for angular contact ball bearing, the ratio of Ball Angular Velocity (δ^\bullet) and Total Speed of the Bearing (S) at each ball-race contact in the rolling direction (j_n) gives Basic Speed Ratio. Solving the ratio of the definition gives the same results as our integrated model.

8.2.6 Spin-Precession Ratio

The influence of spin and precession motions on the angular velocity of the ball is determined by the ratio $\frac{s}{p}$. For a free or Poincot precession (i.e., if the net external moment on the ball is close to zero) p , s and θ are related to the ratio $\frac{s}{p}$.

Table 16 Influence of spin and precession on ball velocity

SPIN-PRECESSION RATIO			UNITS
ratio $(I_E - I_H)/I_E$	$\frac{I_E}{I_E - I_H}$	-0.06	kg/mm ²
SPIN-PRECESSION RATIO	$\frac{s}{p}$	-0.05	-

I_H and I_E are ball inertias along and normal to the axis of the figure. The inertial ratio is assumed based on our experimental investigation. The resultant ratio $\frac{s}{p} = -0.05$ is very small and shows that most of the ball surface velocity comes from the precessional component of angular velocity. In any case, if the precessional motion is not present (pure spin), the ratio indicated that all surface velocities must of course come from spin. Also, Since $I_H > I_E$, spin and precession point more or less in opposite directions and the precession is “retrograde”

8.2.7 Transverse Precessional Slip

The time-varying transverse precessional slip field at outer and inner ball-race contact is estimated. Without this slip field, precession motion can't occur. These slip fields are formed at both inner and outer ball-race contact across the rolling direction (k_n) for the precessional motion to occur.

Table 17 Transverse Precessional Slip Fields at Ball-Race contacts

TRANSVERSE PRECESSIONAL SLIP (along k_n)	UNITS
Transverse Slip at Outer Ball-Race Contacts	0.19 mm/min
Transverse Slip Inner Ball-Race Contacts	-0.19 mm/min

The results from the table evidence that the magnitudes of the transverse slip at ball-race contacts are very very small. It's comprehensible, as most of the ball angular velocity comes from the precessional component while the spin component is almost negligible. Also, they are equal and opposite i.e, they form sinusoidal wave patterns at the rate of precession.

In support of the comments on the EHD slip field already discussed in chapter 3, both transverse and circumferential slip fields at ball-race

contacts are Lubricant Shear Phenomena. They differ from traditional slip fields. Neither of them predicts lock-up in the Hertz zone.

8.2.8 Ball Spin Frequency

All the fundamental defect frequencies calculated by the solver are reported.

Table 18 All the fundamental defect frequencies

BALL SPIN FREQUENCY			UNITS
Number of Balls	N	7.00	units
Contact Angle	B or ϕ	20.00	°
Rotating Unit Frequency or Shaft Speed	F	11.50	Hz
Fundamental Train Frequency	FTF	4.69	Hz
Ball Pass Frequency of the Outer Race	$BPFO$	2.85	Hz
Ball Pass Frequency of the Inner Race	$BPMI$	4.15	Hz
To Verify: Always $BPFO+BPFI=n$		7.00	-
Ball Spin Frequency	BSF	2.46	Hz
Element Defect Frequency	EDF	4.91	Hz

Based on the geometrical parameters of the bearing used in our test rig campaigns, the defect frequencies are numerically estimated by the solver. Other than ball spin frequency, all the other calculated frequencies are just reported for the sake of reference. They have little to no influence on our Integrated Life Model as our model focuses only on the bearing rolling element. The cage and race frequencies are neglected. However, those

frequencies help verify the calculations. Always the sum of **BPFO** and **BPFI** should constitute n . The results of our model verify this condition.

BSF is estimated at 2.46 Hz, which is the total number of cycles in which a ball rotates during a complete shaft cycle, assuming no slip. For every rotation of the rolling element (ball) the defect hits once both to outer and inner race respectively i.e fault in the ball strikes twice this calculated frequency, once the inner race and once the outer race.

The angle B varies with the position of each rolling element in the bearing as the local radial load to axial load ratio changes. Meaning, each rolling element has a different (in direction) effective rolling diameter and each ball tends to rotate at a different speed. The bearing case used in the experimental setup limits the deviation of the rolling elements from their mean position to a great extent. Nonetheless, some random slip is always present since rolling without slip is impossible.

8.2.9 Transverse Slip Ratio

The amount of slip a ball undergoes in one complete shaft revolution is reported. This is calculated by solving the ratio R in the solver.

Table 19 Transverse slip amplitude to ball's surface velocity

TRANSVERSE SLIP RATIO		UNITS
$\frac{\text{Transverse slip amplitude}}{\text{Ball's surface velocity}}$	R	0.023 -

The result of the ratio of transverse slip done by the ball while doing a complete rotation around its principal axis is 0.02. This is calculated by the solver using the formulation of equation 3.17 from chapter 3. According to the literature, this ratio should be $R \approx \frac{1}{100}$.ie transverse slip is about 1% of the ball's surface velocity.

Our developed integrated solver validates this condition. The ratio obtained is 0.023 which is about $\frac{2}{100}$ i.e While Ball did one complete cycle around the principal axis, at the same time also did a transverse slip of about 2/100th of a complete cycle. This can be cross verified by calculating the ratio using the transverse slip and surface velocities reported in the previous tabulations. i.e $R = \frac{\text{transverse slip amplitude}}{\text{ball surface velocity}} = \frac{0.19}{7.15} = 0.023$. This result validates our Integrated Solver again.

As we have mentioned several times already, both transverse and circumferential slip fields at ball-race contacts are Lubricant Shear Phenomena. They differ from traditional slip fields. Neither of them predicts lock-up in the Hertz zone. Uniform slip field is about 1% of the surface velocity in circumferential direction over the whole Hertz area.

Summing up the discussion on this same topic from chapter 3, based on similar experiments done for pure spin (without precession motion), showed the Circumferential slip was also about 1% of surface velocity. It can be speculated that both the slip fields may be present in a Precessing bearing: a time-varying transverse slip superimposed on a uniform drag-induced circumferential slip. A maximum EHD pivoting slip of the same order can also be assumed. All these three slip fields may be involved in a shear-activated lubricant degradation process.

This sudden onset of precession might seem a large and violent change from an existing pure spin. Interestingly, the required additional precessional slips are of the same order as pre-existing drag slips. However, most of the ball surface velocity changes from a rotation about an axis (spin) to a conical motion of the axis (precession). The spin component of angular velocity suffers an order-of-magnitude diminution and an almost complete reversal in direction, yet the slip velocities are not much changed at ball-race contact.

8.2.10 Inclusion Loading Frequency

The result of the frequency with which the defect hit the raceways is reported.

Table 20 Inclusion Loading Frequency (I_L)

INCLUSION LOADING FREQUENCY			UNITS
$\frac{\text{Shaft revolution}}{\text{transverse slip}}$	$\frac{1}{R}$	40.22	-
Inclusion Loading Frequency	I_L	20	-

Assuming that the transverse slip is not random, but always in the same direction of rotation, Micro-inclusion loading frequency. i.e., how frequently the inclusion in the ball contacts the raceways is calculated. Considering that the inclusion is loaded twice during a complete rotation (once with inner race and once with outer race), the micro-inclusion loading frequency would be once half of $\frac{1}{R}$ shaft revolutions. It was furthermore assumed that the load is effective on damaging the rolling element only if the contact occurs when the microinclusion is exactly below the contact point.

8.2.11 Dynamic load capacity&Ball-Race Conformity effects

After the calculation of the Inclusion loading frequency, the next step is to relate the precession motion with the bearing life in the presence of the defect. As we have already discussed, the crucial parameter that helps in relating the precessional slip and micro-inclusion effect with the bearing rolling-element life is the “Equivalent dynamic Load (P_{eq})”. This parameter is present in the bearing life formulation of the Zaretsky model (eqn 2.24 from chapter 2)

Apart from the P_{eq} , there are other parameters in the life formulation which entail being estimated for bearing life estimation. One of them is Dynamic load capacity C_d and the other is the correction introduced called Bearing life factor LF_c .

Table 21 Dynamic load capacity and Bearing life factor

DYNAMIC LOAD CAPACITY & BEARING LIFE FACTOR			UNITS
Material Geometry Co-efficient	f_{cm}	88.00	-
No of Rows of Rolling Elements	j	1.00	units
Dynamic Load Capacity	C_d	30569.98	N
Bearing Envelope Size	S	0.18	-
Ball-Race Conformity Effect			
Critical Shear Stress-Life Exponent	c	10.33	-
Weibull Slope	e	0.60	-
Hertz Stress Life Component	n	13.66	-
Ball Inner Race Conformity Effect	LF_i	29.27	-
Ball Outer Race Conformity Effect	LF_o	1.00	-
Outer to Inner Life Ratio	X	0.50	-
Bearing Life Factor	LF_c	3.10	-

The conformity f of the races, defined as $f = \frac{R_r}{d}$, where R_r is the race radius and d is the ball diameter. It varies between 0.505 and 0.570. For the

investigated bearings, its value is 0.505 for inner race-ball conformity and 0.520 for outer race-ball conformity. These values are obtained from Table 4. Effect of race conformity and Hertz stress-life exponent n on ball-bearing life as a function of ball bearing series (24). And material coefficient (f_{cm}) was obtained by linear interpolation of bearing envelope size value from the same article. The other values are calculated by the solver based on the formulations reported in Chapter 2.

8.2.12 Equivalent Tresca stresses - failed specimens

The equivalent Tresca stresses corresponding to the micro-inclusions dimensions, shape, chemical composition, and depth are calculated using Eshelby's code.

Table 22 Equivalent Tresca Stresses

σ_{nT} [MPa]	σ_{iT} [MPa]	σ_{inc} [%]
501	683	36
577	787	36
555	756	36
539	652	21
591	805	36
580	791	36
563	767	36

For each micro-inclusion found in the failed specimens, the maximum equivalent Tresca stress in the uniform matrix σ_{nT} and at the micro-

inclusion boundary σ_{iT} is calculated based on the micro-inclusions dimension, shape, aspect ratio, position, and elastic modulus. The percent difference σ_{inc} between the two stress values reported as well. The maximum Tresca equivalent stresses σ_{nT} and σ_{iT} calculated at the inclusion depth was assuming the absence and the presence of the inclusion respectively.

8.2.13 Equivalent Tresca stresses - Failed balls

The corrected equivalent Tresca stresses corresponding to the analysis of the Twelve broken balls coming from the test rig are reported. The calculated equivalent stresses are corrected taking into account the composition, location, and dimension of the inclusions experimentally found.

Table 23 Corrected Equivalent Tresca stresses - Failed balls

σ_{nT} [MPa]	σ_{iT} [MPa]	σ_{inc} [%]
1836	2776	51
1550	2158	39
1462	2245	54
2320	3160	36
1886	2290	21
2210	2969	34
1846	2206	20
1384	1728	25
2034	2552	25
1508	1768	17
1616	2200	36
2208	2737	24

8.2.14 Calculated Equivalent Loads

The calculated equivalent loads are reported.

Table 24 Calculated Equivalent Loads

N_L	P_{eqn}	T_L	F_{aa}	L_H	P_{eqi}
[N]	[N]	[N]	[N]	[N]	[N]
34400	22704	74445	8882.3	6100	5862.3
34400	22704	59800	8150.0	4900	5379.0
34400	22704	39053	7112.7	3200	4694.3
34400	22704	75666	8943.3	6200	5902.6
34400	22704	48817	7600.9	4000	5016.6
34400	22704	67123	8516.2	5500	5620.7
34400	22704	47596	7539.8	3900	4976.3
34400	22704	48817	7600.9	4000	5016.6
34400	22704	53698	7844.9	4400	5177.6
34400	22704	45155	7417.8	3700	4895.7
34400	22704	58580	8089.0	4800	5338.7
34400	22704	54919	7906.0	4500	5217.9

N_L is the axial load applied to the bearing during the test rig during experimental testing. L_H is the Hertz Load i.e the contact load applied to a single, homogeneous ball, generating at the microinclusion depth the same Tresca stress due to microinclusions. (P_{eqn}) is the nominal equivalent load. (P_{eqi}) is the dynamic equivalent load that includes the influence of the precessional slip, as well as the micro-inclusion effect. F_{aa} is the weighted average of the nominal load N_L applied to the bearing and the Tresca Load (T_L). P_{eqn} is calculated as per the catalog indication i.e i.e. 0.66 times the axial force acting on the bearing. Similarly, P_{eqi} is 0.66 times the F_{aa} .

8.2.15 Predictions vs Actual Ball Life.

Finally, the bearing life prediction L_{10} calculated by the Integrated Solver are reported

Table 25 Bearing ball life Comparisons

L_{10n}	L_{10i}	N_f
(10^6 Cycles)	(10^6 Cycles)	(10^6 Cycles)
1.97	0.64	0.46
1.97	0.82	1.4
1.97	1.24	1.94
1.97	0.62	0.87
1.97	1.02	1.45
1.97	0.72	0.46
1.97	3.47	3.75
1.97	1.02	1.28
1.97	0.92	0.61
1.97	1.09	0.97
1.97	0.84	0.54
1.97	0.90	0.87

Nominal bearing life L_{10n} assuming the absence of the precessional slip and the micro-inclusion effect corresponding to P_{eqn} is calculated. Likewise, L_{10i} is the bearing life estimated in the presence of micro-inclusion under the influence of the precessional slip, corresponding to P_{eqi} . These predicted ball lives are compared with the experimental cycles of failure (N_f). (N_f) is the actual fatigue life of the ball obtained from experimental investigations. For ease of reference, the values of L_{10} are reported in cycles rather than millions of cycles.

Chapter 9

Conclusions

The objective of the thesis was to evaluate the influence of the Precessional Slip on the life of bearing rolling elements in the presence of micro-inclusions. An Integrated Life Estimation Model with a dedicated Numerical Solver was developed. Based on the geometrical parameters of SKF BAHB-311396B Ball Bearing (Ball material: 100Cr6) obtained from experimental data, all the conditions leading to the precessional slip in terms of the angular velocity of the precessing ball, surface and slip velocities at ball-race contact, spin-precession ratio, ball spin frequency, and inclusion loading frequency were calculated. Corresponding to the fracture analysis data regarding the inclusion's composition, dimension, depth, and aspect ratio, corrected equivalent Tresca stresses were calculated. The fatigue life of the bearing rolling element was obtained from the results of the Test Rig campaigns.

The parameter that is crucial in relating the bearing life with precessional slip and micro-inclusion effect, (P_{eq}) from the Zaretsky life model, was modified to include the average normal force acting on the ball in the presence of micro-inclusion while undergoing transverse precessional

slip. The correction factor accounting for ball-race conformity defects was also introduced. Both nominal bearing life prediction (L_{10n}) and the bearing life prediction (L_{10i}) estimated in the presence of precessional slip and micro-inclusion effect was calculated using the solver.

The results of bearing's ball life predictions from the solver (both L_{10} and L_{10i}) were compared with the actual experimental fatigue test rig results of the ball (N_f). The L_{10} results calculated by our solver were amazingly accurate and closest to the actual experimental cycles of failure (N_f). There was a clear distinction between the results obtained from the nominal bearing life estimation model L_{10n} and our integrated bearing life estimation model L_{10i} when compared with (N_f). The propinquity or the closeness between results of bearing's ball life estimated based on integrated life model and the actual experimental campaigns validates our integrated solver-based model.

Chapter 10

Future Works

In the analysis of the ball precessional motion, a reference system modeling the local reference frame is presented. This reference system is modeled for full complement retainer less angular contact bearing (29). But in our experimental setup, a cage or retainer was introduced to limit the deviation of the rolling element from its mean position to avoid any random slip. Also, our experimental setup was modeled to focus the failure on the rolling element (ball). This was done by modifying the bearing by removing some balls. Due to lack of experimental data, The full complement bearing reference system was assumed to our model as well.

In the experiment of Figure 1 (28), by solving the expressions based on typical bearing parameters given, the precession angle is approximated to $\theta = 10^\circ$. According to (37), the precession angle is strongly dependent on lubrication conditions. Experimentally, the precession angle can be measured through a stroboscope. Due to the lack of detailed experimental measurements and also considering the different testing conditions and different lubricant properties, the precession angle θ was assumed to be 30° in our experimental setup.

Slip, Entrainment, and Contact velocities at Ball-Ball contact are determined for Retainerless Ball Bearing in (29). Since the bearing used in our experimental setup is a Retainer Bearing, the calculations on contact, slip, and entrainment velocities at Ball-Ball contact were neglected.

Further discussions and further developments on these assumptions can improve the conditions leading to the precessional slip and as a whole, more accurate bearing rolling element estimation models.

Bibliography

1. *The relationship between 100Cr6 steelmaking, inclusion microstructure and rolling contact fatigue performance.* **H, Fu.** s.l. : Int J Fatigue, 2019.

2. *An approach to investigating subsurface fatigue in a rolling/sliding contact.* **Savolainen M, Lehtovaara A.** s.l. : Int J Fatigue 2018.

3. *A coupled damage model and a semi-analytical contact solver to simulate butterfly wing formation around non-metallic inclusions.* **Beyer T, Sadeghi F, Chaise T, Leroux J, Nelias D.** s.l. : Int J Fatigue, 2019.

4. *Effect of non-metallic inclusion on butterfly wing initiation crack formation, and spall geometry in bearing steels.* **SM, Moghaddam.** 2015, Int J fatigue, p. 203-15.

5. *A 3D numerical and experimental investigation of microstructural alternations around non-metallic inclusions in bearing steel.* **Moghaddam SM, Sadeghi F, Paulson K, Weinzapfel N, Correns M, Dinkel M.** s.l. : Int J Fatigue, 2016, p. 29-41.

6. *Effects of non-metallic inclusions on the crack propagation in bearing steel.* **Guan J, Wang L, Zhang C, Ma X.** s.l. : Tribol Int, 2017.

7. *Influence of inclusion pairs, clusters and stringers on the lower bound of the endurance limit of bearing steels.* **Courbon J, Lormand G, Dudragne G, Daguier P, Vincent A.** s.l. : Tribol Int, 2003.

8. *Die Lebensdauer von Kugellagern (The Service Life of Ball Bearings).* **A, Palmgren.** s.l. : NASA TT-F-13460, 1924.

9. *Dynamic capacity of rolling bearings.* **Lundberg G, Palmgren A.** s.l. : Acta Polytechnica Mechanical Engineering Series, 1947.
10. *Über die berührung elastischer körper (On contact of elastic bodies).* **Hertz, H.** s.l. : Gesammelte Werke (Collected Works),, 1881.
11. *Investigators of rolling bearings at SKF Industries, Inc., Review of current and anticipated lubricant problems in turbojet engines.* **Styri, H.** s.l. : NACA Subcommittee on Lubrication and Wear, NACA RM 51D20, 1951.
12. *A Palmgren revisited – A basis for bearing life prediction.* **E.V, Zaretsky.** s.l. : Lubrication Engineering, J. STLE, 54(2), 1998, p. 18-24.
13. *STLE life factors for rolling bearings STLE SP-34, Society of Tribologists and Lubrication Engineers.* **Zaretsky, E.V.** STLE SP-34, Society of Tribologists and Lubrication Engineers, s.l. : Park Ridge, 1992.
14. *Reports from the central laboratory for scientific investigation.* **Stribeck, R.** s.l. : ASME Trans, 1900, p. 420–466.
15. *Ball and Roller Bearing Engineering.* **Palmgren, A.** s.l. : 1st ed., Translation by G. Palmgren and B. Ruley, SKF Industries , 1945.
16. *Dynamic capacity of roller bearings.* **Lundberg G, Palmgren A.** s.l. : Acta Polytechnica Mechanical Engineering Series, 1952, p. 2, 4.
17. *A Physically based model for endurance limit of bearing steels.* **Harris, E. Ioannides and T.A.** s.l. : Journal of Tribology, 1985.
18. *A new fatigue life model for rolling bearings.* **T.A., Ioannides E and Harris.** 1985, p. 367-378.

19. *A study on P-S-N curve for rotating bending fatigue test for bearing steel.* **Tosha, K., Ueda, D., Shimoda, H., and Shimizu, S.,** s.l. : Tribology Trans., 2008, p. 166–172.
20. *Life Ratings for Modern Rolling Bearings: A Design Guide for the Application of International Standard ISO 281/2.* **Division, ASME Tribology.** s.l. : American Society of Mechanical Engineers, 2003.
21. *Rolling Bearings – Dynamic Load Ratings.* **2:2000, ISO 281:1990/Amd 1 and.** s.l. : International Organization for Standardization,, 2002.
22. *Rolling Bearings – Dynamic Load Ratings and Rating Life.* **ISO 281:2007, 2007.** s.l. : International Organization for Standardization, 2007.
23. *Reexamination of ball-race conformity effects on ball bearing life.* **Zaretsky, E.V., Poplawski, J.V., and Root, L.E.,** s.l. : Trib. Trans., 50(3),, 2007, p. 336–349.
24. *Rolling bearing life prediction, theory, and application.* **Zaretsky, Erwin V.** s.l. : Recent Developments in Wear Prevention, Friction and Lubrication, 2010: 45-136, p. 77.
25. *Fatigue criterion to system design, life and reliabilit.* **Zaretsky, E.V.,** s.l. : AIAA Journal of Propulsion and Power, 1987, p. 76-83.
26. *Design for life, plan for death.* **Zaretsky, E.V.** s.l. : Machine Design, 66(15),, p. 55–59.
27. *Relation between Hertz stress-life exponent, ball-race conformity, and ball bearing life.* **Zaretsky, E.V., Poplawski, J.V., and Root, L.E.,** s.l. : Tribol. Trans., 51(2),, p. 150–159.

28. *Ball motion in angular contact bearings.* **EP, Kingsbury.** s.l. : Instrumentation Laboratory, Massachusetts Institute of Technology, Cambridge, Mass. (U.S.A.), 1967, Vol. Wear 1978.

29. *Precessional Slip in Angular Contact Bearing.* **P., Kingsbury E.** s.l. : Bearing Center, The Charles Stark Draper Laboratory, Inc., Cambridge, MA, 1981, Vol. Wear, 77 (1982), p. 105 - 114.

30. **H. L. Heathcote.** s.l. : *Mech World*, 70, 1921, p. 79.

31. *A general theory for elasticity constrained ball and radial roller bearings under arbitrary load and speed conditions.* **Jones, A. B.** s.l. : *J. Basic Eng.*, 3, 1960, p. 309.

32. *Rolling Bearing Analysis.* **T. A. Harris.** 1966, Vol. Wiley, New York.

33. *The analysis of the motion of balls in an unlubricated angular contact thrust ball bearing.* **Kalker, J. J.** s.l. : *Wear*, 12, 1963, p. 3.

34. *Angular contact ball bearings: track position at high speeds.* **E. P. Kingsbury, K. C. Falcon and C. Andrew, Proc.** s.l. : *Inst. Mech. Eng.*, 1970, Vol. 184, p. 24.

35. *Microslip and creep in contacts.* **Poritsky, H.** s.l. : *NASA Spec. Publ.*, 1970.

36. *Slip measurement in an angular contact ball bearing,* **ASME. Kingsbury, E. P.** s.l. : *ASME Paper 81-Lub-33*, 1981.

37. *Ball motion in angular contact ball bearings.* **E. P. Kingsbury.** s.l. : *Wear*, 11, 1968, p. 41.

38. *Ball motion perturbation in an angular contact ball bearing.* **Kingsbury, E. P.** s.l. : *ASLE Paper 81-AM-1E-1*.

39. Basic speed ratio of an angular contact bearing,. **E. P. Kingsbury**.
s.l. : J. Lubr. Technol, 1980, p. 391.

40. Dynamic and coupling influences on basic speed ratio of an angular contact ball bearing,. **E. P. Kingsbury**. s.l. : Wear, 63, 1980, p. 189.

41. Ball Bearing Fault Detection Using Vibration Parameters. **Surojit Poddar, Madan Lal Chandravanshi**. Dhanbad, Jharkhand,India. : Department of Mechanical Engineering, Indian school of Mines, .

42. Rolling element bearing diagnostics - A tutorial. **Randall, Robert B**. Sydney : School of Mechanical and Manufacturing Engineering, University of New South Wales.

43. Lubricant breakdown in instrument ball bearings,. **E. P. Kingsbury**.
s.l. : J. Lubr. Technol.,, 1978, p. 386.

44. Lubricant breakdown acceleration in instrument ball bearings,. **E. P. Kingsbury**. s.l. : Hughes Aircraft Co, 1979, Vol. 5th Inertial Guidance Community Contamination Control Semin.

45. The determination of the elastic field of an ellipsoidal inclusion, and related problems. **JD, Eshelby**. 241(1226), s.l. : Proc R Soc London Ser A Math Phys Sci, 1957, p. 376–96.

46. Effect of defect shape on rolling contact fatigue crack initiation and propagation in high strength steel. **T, Makino**. s.l. : Int J Fatigue Nov. , 2016, Vol. 92:507–16.

47. Influence of hydrogen trapped by inclusions on fatigue strength of bearing steel. **Murakami Y, Yokoyama N**. s.l. : In: Bearing Steel Technology, ASTM International, 2009, p. 113–12.

49. *Study of rolling contact fatigue of bearing steels in relation to various oxide inclusions.* **Hashimoto K, Fujimatsu T, Tsunekage N, Hiraoka K, Kida K, Santos EC.** 2011.
50. **Morosi, Francesco.** *Effect of microinclusions on the fatigue life of rolling bodies.* 2017.
51. *The fatigue limit of bearing steels – Part II: Characterization for life rating standards.* **Gabelli A, Lai J, Lund T, Rydén K, Strandell I, Morales-Espejel GE.** s.l. : *Int J Fatigue*, 2012, p. 169–80.
52. *Influence of microinclusion in life of rolling elements: Experimental, microstructural, analytical and numerical investigation.* **R. Sesana, E. Ossola, S. Pagliassotto, S. Rizzo, E. Brusa.** s.l. : *International Journal of Fatigue* Volume 139, 2020.
53. *Standard Test Methods for Determining the Inclusion Content of Steel. E45-18a, ASTM.* s.l. : *ASTM Int. Conshohocken, PA.,* 2018.
54. *Micromechanics of defects in solids.* **Mura T, Barnett DM.** s.l. : *J Appl Mech*, 1983.
55. *Two-ellipsoidal inhomogeneities by the equivalent inclusion method.* **Moschovidis ZA, Mura T.** s.l. : *J Appl Mech Trans ASME*, 1975.
56. *Elliptic integrals and functions.* **M, Igor.** s.l. : *Mathworks*, 2015.
57. *Evaluation of the Eshelby solution for the ellipsoidal inclusion and heterogeneity.* **W, Pollard D. D. Meng C. Heltsley.** s.l. : *Computers and Geosciences*, 2011.
58. *Elastic field in 3D due to a spheroidal inclusion- MATLAB code for Eshelby's.* **D., Healy.** s.l. : *Computers and Geosciences*, 2008.

59. *Inclusion Rating by Statistics of Extreme Values and Its Application to Fatigue Strength Prediction and Quality Control of Materials.* **Murakami, Y.** s.l. : *Journal of Research of the National Institute of Standards and Technology*, 1994.

60. *Characterization of inclusions in clean steels:a review including the statistics of extremes methods.* **H.V. Atkinson, G. Shi.** s.l. : *Department of Engineering Materials, University of Sheffield*, 2002.